Tesi doctoral presentada per En/Na

Marc PERA TITUS

amb el títol

"Preparation, characterization and modeling of zeolite NaA membranes for the pervaporation dehydration of alcohol mixtures"

per a l'obtenció del títol de Doctor/a en

QUÍMICA

Barcelona, 29 de maig del 2006

Facultat de Química
Departament d'Enginyeria Química

UNIVERSITAT DE BARCELONA

This chapter presents a new method to characterize pore size distributions (PSDs) in UF, NF and MF (meso- and macroporous) asymmetric membranes from flux measurement by applying moment theory, which is validated with experimental data obtained in our laboratory. The method is extended to characterize large defects (meso- and macroporous) in composite zeolite NaA membranes from VPV measurements, which might be responsible for the reduction of selectivity towards dehydration. The method allows the determination of a mean pore size and an intercrystalline porosity, which reveals as a valuable tool for directing synthesis strategies in the preparation of zeolite membranes.

VI.1. CHARACTERIZATION OF PSDs IN NF, UF AND MF MEMBRANES: MOMENT THEORY

Commercial UF, NF and MF porous membranes supplied by manufacturers usually consist of an active top layer deposited or grown onto a much thicker porous support (e.g., composite zeolite NaA membranes, see chapter IV). This porous top layer can be visualized as an array of parallel and cylindrical pores of size **d** [m]. In a first approach, any possible contribution of the bulk support is omitted. Irrespective of its actual functional dependence on the pore size, a PSD can be defined in terms of a continuous number pore size density function, $\boldsymbol{\varepsilon(d)}$, which is defined in such a way that the fraction of porosity lying in the range **d** and $\boldsymbol{\delta d}$ is $\boldsymbol{\varepsilon(d)\,\delta d}$. It should be stressed that the density function $\varepsilon(d)$ has been chosen not normalized to 1, so that it might account for the total porosity of the membrane layer. Furthermore, the cumulative PSD, $\boldsymbol{E(d^*)}$, is defined as the fraction of porosity found for pore sizes ranging from 0 to d^* (Eq. VI.1)

$$E(d^*) = \int_0^{d^*} \varepsilon(d)\,\delta d \qquad \text{(Eq. VI.1)}$$

The statistical moments $\langle \mathbf{d}^{\mathbf{i}} \rangle$ of a PSD characterized by a density function $\varepsilon(d)$ can be generated by Eq. VI.2

$$\langle d^i \rangle = \int_0^{\infty} d^i\, \varepsilon(d)\,\delta d \ \ [m^i] \quad \text{for } i = -\infty, \ldots, -2, -1, 0, 1, 2, \ldots, +\infty, \qquad \text{(Eq. VI.2)}$$

In a subsequent step, a number of mean pore sizes, $\boldsymbol{\bar{d}_i}$ [m], can be defined from the statistical moments $\langle d^i \rangle$ and $\langle d^{i-1} \rangle$, which allow the determination of the function $\varepsilon(d)$ by Eq. VI.3

$$\bar{d}_i = \frac{\langle d^i \rangle}{\langle d^{i-1} \rangle} = \frac{\int_0^{\infty} d^i\, \varepsilon(d)\,\delta d}{\int_0^{\infty} d^{i-1}\, \varepsilon(d)\,\delta d} \qquad \text{(Eq. VI.3)}$$

It should be highlighted that the knowledge of a higher number of mean pore sizes, $\bar{d}_i$, allows a more accurate description of the function $\varepsilon(d)$, which in its turn implies the knowledge of a higher number of its statistical moments. Our interest focuses on the possibility of relating these moments to some physical properties or permeation fluxes, which constitute the subject of discussion of section VI.1.1.

VI.1.1. Statistical moments of a PSD

VI.1.1.1. 0th moment

The 0th moment of the distribution $\varepsilon(d)$, $\langle \mathbf{d}^{\mathbf{0}} \rangle$ [-], can be directly obtained from Eq. VI.2 on the basis of its relationship with the total porosity of the membrane, $\boldsymbol{\varepsilon_T}$ [-] , by Eq. VI.4

$$\left\langle d^0 \right\rangle = \int_0^\infty d^0 \, \varepsilon(d) \, \delta d = \int_0^\infty \varepsilon(d) \, \delta d = \varepsilon_T \quad [-] \qquad \text{(Eq. VI.4)}$$

VI.1.1.2. 1st and 2nd moments

In addition to the 0th moment, the 1st and 2nd moments of $\varepsilon(d)$, $\langle \mathbf{d}^{\mathbf{1}} \rangle$ [m] and $\langle \mathbf{d}^{\mathbf{2}} \rangle$ [m^2], can be calculated, respectively, from pure *Knudsen* diffusion and pure pressure-driven *viscous* or *Poiseuille* fluxes, on the basis of their different functional dependence on the PSD of a membrane, since the mass transfer mechanisms involved are also different. The relative contribution of each mechanism to the overall mass transfer across a membrane depends on the mean-free path of the permeating molecules, λ [m], which is defined as the mean distance that a molecule runs between two consecutive collisions (see section I.2.2). For ideal gases, it can be calculated by Eq. VI.5 (or Eq. I.1)

$$\lambda = \frac{1}{\sqrt{2\pi d_m^2}} \frac{RT}{P_m N_A} \quad [m], \qquad \text{(Eq. VI.5)}$$

where $\mathbf{d_m}$ [m] is the kinetic diameter of the molecules, $\mathbf{N_A}$ [-] is the Avogadro Number and $\mathbf{P_m}$ [Pa] is the mean pressure between the feed and permeate sides of the membrane. The pure Knudsen diffusion flux takes place preferentially through a membrane pore when its size is much lower than λ, being the frequency of collisions with the pore wall higher than with other molecules. On the other hand, the viscous flux is predominant for pore sizes higher than λ and involves a laminar profile inside the pores generated by friction of the permeating molecules with the pore walls. For practical applications, pure Knudsen and pure viscous fluxes take place preferentially, respectively, when the conditions $P_m \, d \leq 0.01$ Pa m and $P_m \, d \geq 0.1$ Pa m are fulfilled (*Levenspiel, 1999*).

For the special case that the density function $\varepsilon(d)$ of the PSD of a membrane can be described by a narrow unimodal or δ-Dirac function, all the mean pore sizes tend to a fix value, $\bar{d}$ (i.e. $d = \bar{d}$, $\varepsilon(d) = \varepsilon_T$; $d \neq \bar{d}$, $\varepsilon(d) = 0$). For this particular situation, pure Knudsen and viscous fluxes, $\mathbf{N_G^{Kn}}$ and $\mathbf{N_G^{V}}$ for single-gas permeance across the z-direction of the membrane can be accounted for, respectively, by Eqs. VI.6 and VI.7, in a similar manner as was pointed out in section III.2.1.1 for the determination of viscous or laminar contributions in *as*-synthesized zeolite NaA membranes

$$N_G^{Kn} = -\frac{\varepsilon_T}{\tau}\frac{D_{Kn}}{RT}\frac{\delta P}{\delta z} = \frac{\varepsilon_T\,\bar{d}}{3\tau\ell}\sqrt{\frac{8}{\pi M RT}}\Delta P \quad [\text{mol m}^{-2}\text{ s}^{-1}] \qquad \text{(Eq. VI.6)}$$

$$N_G^{V} = -\frac{\varepsilon_T}{\tau\ell}\frac{\bar{d}^2}{32\mu_G}\frac{P_m}{RT}\frac{\delta P}{\delta z} = \frac{\varepsilon_T}{\tau\ell}\frac{\bar{d}^2}{32\mu_G}\frac{P_m}{RT}\Delta P \quad [\text{mol m}^{-2}\text{ s}^{-1}], \qquad \text{(Eq. VI.7)}$$

where $\boldsymbol{\tau}$, $\boldsymbol{\ell}$ and $\mathbf{\Delta P}$ are, respectively, the tortuosity [-], the membrane thickness [m] and the transmembrane pressure [Pa]. The extension of Eqs. VI.6 and VI.7 to the general case that a the density function $\varepsilon(d)$ differs from a δ-Dirac function, the 1st and 2nd moments of $\varepsilon(d)$ can be calculated, respectively, by Eqs, VI.8 and VI.9

$$\left\langle d^1\right\rangle = \int_0^\infty d^1\,\varepsilon(d)\,\delta d = 3\tau\ell\sqrt{\frac{\pi MRT}{8}}\frac{N_G^{Kn}}{\Delta P} = 3\tau\ell\sqrt{\frac{\pi MRT}{8}}\,Q_G^{Kn} \text{ [m]} \qquad \text{(Eq. VI.8)}$$

$$\left\langle d^2\right\rangle = \int_0^\infty d^2\,\varepsilon(d)\,\delta d = \tau\ell\frac{32\mu_G\,RT}{P_m}\frac{N_G^{V}}{\Delta P} = \tau\ell\frac{32\mu_G\,RT}{P_m}Q_G^{V} \text{ [m}^2\text{]}, \qquad \text{(Eq. VI.9)}$$

where $\mathbf{Q_G^{Kn}} = N_G^{Kn}/\Delta P$ and $\mathbf{Q_G^{V}} = N_G^{V}/\Delta P$, both in [mol m^{-2} s^{-1} Pa^{-1}], correspond, respectively, to the pure Knudsen and pure viscous gas permeances. Note that the Knudsen gas permeance is independent of pressure. From Eqs. VI.8 and VI.9, pure Knudsen and viscous gas permeances can be rewritten in the general form:

$$Q_G^{Kn} = \Psi\left\langle d^1\right\rangle = \Psi\int_0^\infty d^1\,\varepsilon(d)\,\delta d \qquad \text{(Eq. VI.10)}$$

$$Q_G^{V} = \Phi\,P_m\left\langle d^2\right\rangle = \Phi\,P_m\int_0^\infty d^2\,\varepsilon(d)\,\delta d, \qquad \text{(Eq. VI.11)}$$

with $\Psi = \left(\frac{1}{3}\frac{D_{Kn}}{RT}\right)\left(\frac{1}{\tau\ell}\right)$ [mol m^{-3} s^{-1} Pa^{-1}] and $\Phi = \left(\frac{D_V}{RT}\right)\left(\frac{1}{\tau\ell}\right)$ [mol m^{-4} s^{-1} Pa^{-2}]

In the most general situation that Knudsen and viscous gas fluxes occur simultaneously, the overall mass transfer across a membrane is described by the sum of Eqs. VI.9 and VI.10:

$$Q_G^{T} = Q_G^{Kn} + Q_G^{V} = \Psi\left\langle d^1\right\rangle + \Phi\,P_m\left\langle d^2\right\rangle = \int_0^\infty\left(\Psi\,d^1 + \Phi\,P_m\,d^2\right)\varepsilon(d)\,\delta d \qquad \text{(Eq. VI.12)}$$

For the special case that a pure liquid (e.g., water) permeates across the membrane, only pressure-driven flux can be attained. For such a situation, Eq. VI.9 transforms into Eq. VI.13

$$\left\langle d^2 \right\rangle = \int_0^\infty d^2\, \varepsilon(d)\, \delta d = \tau\, \ell\, \frac{32\, M\, \mu_L}{\rho_L}\, \frac{N_L^V}{\Delta P} = \tau\, \ell\, \frac{32\, M\, \mu_L}{\rho_L}\, Q_L^V \quad [m^2], \qquad \text{(Eq. VI.13)}$$

where $\mathbf{N_L^V}$ is the flux of the pure liquid [mol m^{-2} s^{-1}] and $\mathbf{Q_L^V} = N_L^V / \Delta P$ is the pure viscous liquid permeance or permeability [mol m^{-2} s^{-1} Pa^{-1}].

VI.1.1.3. -kth moments (k = 0 → ∞)

Additional statistical moments of the density function $\varepsilon(d)$ can be obtained from the hindered diffusion of a large solute in a liquid solution through a membrane of comparable mean pore size in the absence of viscous flux (i.e. $\Delta P = 0$), which is actually responsible for the sieving ability of a membrane. However, compared to pure Knudsen and viscous fluxes, the relationship between solute diffusive fluxes and the statistical moments is more subtle.

The hindered diffusion of a large solute through a pore is commonly ascribed to a hindered diffusion coefficient which is dependent on the ratio $\mathbf{d_m / d}$. The hindered diffusion coefficient is commonly modeled by means of the Renkin equation (*Pappenheimer et al., 1951*), which was originally formulated on the basis of the diffusion of an uncharged spherical solute through a cylindrical pore. For NF applications, the Renkin equation is often approximated to a ν-exponent power law, where ν commonly takes the number 4 (Eq. VI.14):

$$D\left(\frac{d_m}{d}\right) = D_\infty \left(1 - \frac{d_m}{d}\right)^\nu \quad [m^2\ s^{-1}], \qquad \text{(Eq. VI.14)}$$

where $\mathbf{D_\infty}$ [m^2 s^{-1}] is the diffusivity of a solute in an environment without any interaction with the pore walls (i.e. $d_m / d \to 0$). In fact, the explicit dependence of the hindered diffusivity of a solute on the pore size allows it to act as a moment generating function, as was previously proposed by *Baltus (1997b)*. Hence, the diffusive flux of a solute along the z-direction of a membrane, $\mathbf{N_m^D}$ [mol m^{-2} s^{-1}], with a PSD described by $\varepsilon(d)$ can be modeled by Eq. VI.15

$$N_m^D = \left[\int_0^\infty D\left(\frac{d_m}{d}\right) \varepsilon(d)\, \delta d\right] \frac{\Delta C}{\tau\, \ell} = \frac{D_\infty}{\tau\, \ell} \left[\int_0^\infty \left(1 - \frac{d_m}{d}\right)^\nu \varepsilon(d)\, \delta d\right] \Delta C \quad [\text{mol } m^{-2}\ s^{-1}]$$

(Eq. VI.15)

where $\mathbf{\Delta C}$ [mol m^{-3}] is the solute concentration difference across the membrane. Eq. VI.15 can be rewritten as a function of the statistical moments of $\varepsilon(d)$ by developing Eq. VI.14 in a Mc Laurin series around the point $d_m / d = 0$, which adopts the general form

$$D_\infty \left(1-\frac{d_m}{d}\right)^\nu = D_\infty \left[1-\nu\left(\frac{d_m}{d}\right)^1+\frac{1}{2}(\nu-1)\nu\left(\frac{d_m}{d}\right)^2-\frac{1}{6}(\nu-2)(\nu-1)\nu\left(\frac{d_m}{d}\right)^3+\ldots\right]$$

$$= D_\infty \sum_{k=0}^{\infty}(-1)^k\binom{\nu}{k}\left(\frac{d_m}{d}\right)^k, \qquad \text{(Eq. VI.16)}$$

where, in its turn, the combinatorial numbers can be calculated by Eq. VI.17

$$\binom{\nu}{k} = \frac{\nu!}{k!(\nu-k)!} \qquad \text{(Eq. VI.17)}$$

The substitution of Eq. VI.16 into Eq. VI.15 leads to the explicit dependence of the solute flux through a membrane on the moments of $\varepsilon(d)$:

$$N_m^D = \frac{D_\infty}{\tau\,\ell}\left[\int_0^\infty \sum_{k=0}^{\infty}(-1)^k\binom{\nu}{k}\left(\frac{d_m}{d}\right)^k \varepsilon(d)\,\delta d\right]\Delta C = \frac{D_\infty}{\tau\,\ell}\left[\sum_{k=0}^{\infty}(-1)^k\binom{\nu}{k} d_m^k \left\langle d^{-k}\right\rangle\right]\Delta C$$

(Eq. VI.18)

As can be seen, the solute flux depends on the **-kth** moments of $\varepsilon(d)$ and on a k-power function of $\mathbf{d_m}$. The weight of the kth term depends on the relative value of its corresponding term $\mathbf{d_m^k\ \langle d^{-k}\rangle}$. It should be emphasized that the 0th term of Eq. VI.17 refers to the total porosity of the membrane (i.e. $d_m{}^0\langle d^{-0}\rangle = \langle d^0\rangle = \varepsilon_T$ [-]), which is dominant for a solute with $d_m/d \to 0$. Moreover, Eq. VI.18 also reveals that the term $d_m{}^1\langle d^{-1}\rangle$ actually governs the hindering effect of the pore wall. In fact, the terms related to higher **k** values play a more relevant role for higher d_m/d ratios. For instance, for the diffusion of a solute with d_m/d <0.1 and $\nu = 4$, $(1-d_m/d)^4 \approx 1-4\,(d_m/d)^1$ with a truncation error lower than 10%. Thus, Eq. VI.18 approaches Eq. VI.19 in the calculation of N_m^D:

$$N_m^D \approx \frac{D_\infty}{\tau\,\ell}\left[\int_0^\infty \left(1-4\,d_m^1\,d^{-1}\right)\varepsilon(d)\,\delta d\right]\Delta C = \frac{D_\infty}{\tau\,\ell}\left[\left\langle d^0\right\rangle - 4\,d_m^1\left\langle d^{-1}\right\rangle\right]\Delta C \qquad \text{(Eq. VI.19)}$$

On the other hand, the diffusion of a non-hindered solute ($d_m/d \to 0$) allows the approximation of Eq. VI.18 to Eq. VI.20 through the use of Eq. VI.4 to relate the 0th moment of $\varepsilon(d)$ with the total porosity of the membrane

$$N_m \approx \frac{D_\infty}{\tau\,\ell}\left[\int_0^\infty 1\ \varepsilon(d)\,\delta d\right]\Delta C = \frac{D_\infty}{\tau\,\ell}\left\langle d^0\right\rangle\Delta C = \frac{\varepsilon_T\,D_\infty}{\tau\,\ell}\Delta C \qquad \text{(Eq. VI.20)}$$

Eq. VI.20 allows the direct determination of the term $\varepsilon_T/\tau\,\ell$ [m^{-1}], which provides relevant structural information concerning the thickness of a membrane layer without the need of breaking it for microscopy analysis (e.g., SEM, FESEM, TEM or AFM, see Table I.4).

Moreover, Eq. VI.20 transforms into Eq. VI.21 through the definition of the permeance of the non-hindered solute, $\mathbf{Q_m^D = N_m^D / \Delta C}$ [m s^{-1}], in a similar manner as was pointed out by *Masselin et al. (2000)*

$$\frac{\varepsilon_T}{\tau \ell} = \frac{Q_m^D}{D_\infty} \qquad \text{(Eq. VI.21)}$$

VI.1.1.4. Structural parameters

As was above aforementioned, Eqs. VI.8, VI.9, VI.13 and VI.21 include relevant information concerning the form of the $\varepsilon(d)$ function of the PSD of a membrane. In fact, for practical purposes, the following set of relevant structural parameters, $\mathbf{R}$ [$m^{(1-i)}$], can be experimentally determined (Eqs. VI.22-VI.24), which indicate the resistance offered by the membrane for each mass transfer mechanism

$$R_{M,0} = \frac{\tau \ell}{\langle d^0 \rangle} = \frac{\tau \ell}{\varepsilon_T} \frac{D_\infty}{Q_m^D} \quad [m] \qquad \text{(Eq. VI.22)}$$

$$R_{M,1} = \frac{\tau \ell}{\langle d^1 \rangle} = \frac{1}{3} \sqrt{\frac{8}{\pi M R T}} \frac{1}{Q_G^{Kn}} \quad [-] \qquad \text{(Eq. VI.23)}$$

$$R_{M,2} = \frac{\tau \ell}{\langle d^2 \rangle} = \frac{P_m}{32 \mu_G R T} \frac{1}{Q_G^V} = \frac{\rho_L}{32 M \mu_L} \frac{1}{Q_L^V} \quad [m^{-1}] \qquad \text{(Eq. VI.24)}$$

It should be noted that resistance $\mathbf{R_{M,2}}$ that involves pressure-driven viscous flux can be either experimentally determined by a single-gas permeance experiment for P_m d >0.1 Pa m or by a pure liquid permeability experiment.

VI.1.2. A special case: unimodal log-normal PSDs

If the log-normal PSD in its simplest version (unimodal) is accepted as an approximation to the real PSD of a porous membrane (*Aimar et al., 1990; Cooper and Derveer, 1979; Michaels, 1980*), the flux pattern of the membrane can be easily derived from the earlier considerations. The density function for the log-normal PSD can be described by the bi-parametric Eq. VI.25

$$\varepsilon(d) = \frac{\varepsilon_T}{\pi^{1/2} \beta d} \exp\left\{ -\left[\frac{1}{\beta} Ln\left(\frac{d}{\alpha} \right) \right]^2 \right\} \qquad \text{(Eq. VI.25)}$$

where the parameter **β** measures the breath of the distribution and **α** is the median value of the distribution. It should be noted that Eq. VI.25 has been chosen not normalized to allow the area drawn by this function with the d-axis to account for the total porosity, ε_T, of the membrane. Figure VI.1 plots normalized log-normal PSDs for a given median value of **α** = 50 nm and for **β** values in the range 0.5 – 1.5 nm. As would be expected, wider distributions are obtained for higher β parameters with peaks that tend to lower diameters.

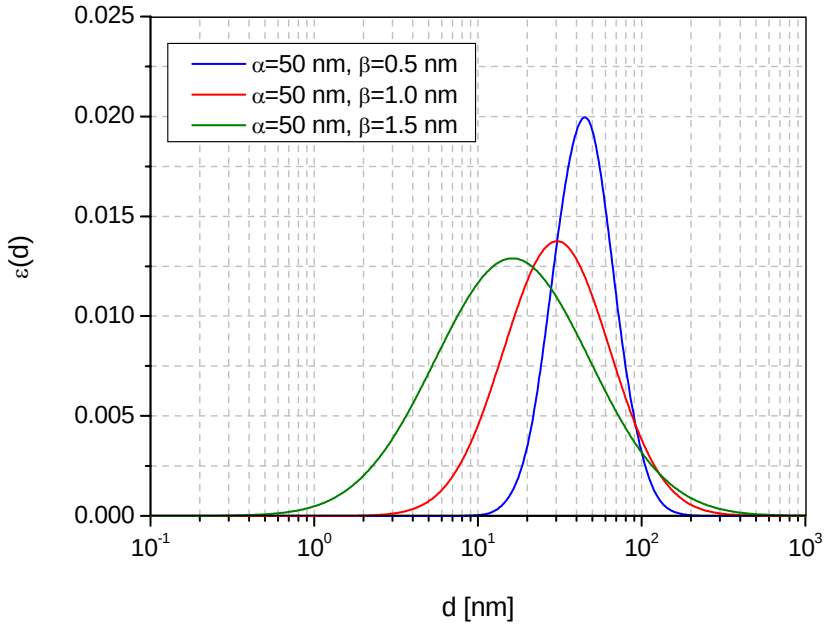

Figure VI.1: Evolution of the normalized log-normal PSD (ε_T = 1) with β parameter for α = 50 nm.

The relevant parameters of a log-normal PSD, **α** and **β**, can be calculated by knowing **only two diameters** of the distribution, $\bar{d}_1$ and $\bar{d}_2$, which imply the knowledge of **only three moments** of the PSD subjected to experimental determination from **three independent permeances**: (1) pure Knudsen diffusion permeance of a single gas (e.g., N_2), pure pressure-driven viscous flux either of a gas or a liquid, and permeance of a target electrolyte (e.g., HCl) by non-hindered diffusion. In this way, using the resistances defined in Eqs. VI.22-VI.24 and a pressure-driven viscous flux experiment carried out for a single gas, diameters $\bar{d}_1$ and $\bar{d}_2$ can be calculated, respectively, by Eqs. VI.26 and VI.27

$$\bar{d}_1 = \frac{\langle d^1 \rangle}{\langle d^0 \rangle} = \frac{\int_0^\infty d^1\, \varepsilon(d)\, \delta d}{\int_0^\infty d^0\, \varepsilon(d)\, \delta d} = \frac{R_{M,0}}{R_{M,1}} = 3\, D_\infty \sqrt{\frac{\pi M}{8RT}}\, \frac{Q_G^{Kn}}{Q_m^D} \quad [m] \qquad \text{(Eq. VI.26)}$$

$$\bar{d}_2 = \frac{\langle d^2 \rangle}{\langle d^1 \rangle} = \frac{\int_0^\infty d^2\, \varepsilon(d)\, \delta d}{\int_0^\infty d^1\, \varepsilon(d)\, \delta d} = \frac{R_{M,1}}{R_{M,2}} = \frac{32}{3} \frac{\mu_G\, RT}{P_m} \sqrt{\frac{8}{\pi M RT}}\, \frac{Q_G^V}{Q_G^{Kn}} \quad [m] \quad \text{(Eq. VI.27)}$$

For the special case of very narrow PSDs ($\beta \to 0$, $\varepsilon(d) \to$ δ-Dirac function), Eq. VI.28 must hold

$$\frac{\left(Q_G^{Kn}\right)^2}{Q_G^V\, Q_m^D} = \frac{256\, \mu_G}{9\, \pi\, M\, D_\infty\, P_m} \quad [\text{mol m}^{-3}\ \text{s}^{-1}\ \text{Pa}^{-1}] \quad \text{(Eq. VI.28)}$$

It should be noted that, if pressure-driven viscous flux experiment is carried out for a pure liquid, Eqs. VI.27 and VI.28 transform, respectively, into Eqs. VI.29 and VI.30

$$\bar{d}_2 = \frac{\langle d^2 \rangle}{\langle d^1 \rangle} = \frac{\int_0^\infty d^2\, \varepsilon(d)\, \delta d}{\int_0^\infty d^1\, \varepsilon(d)\, \delta d} = \frac{32}{3} \frac{M\, \mu_L\, RT}{\rho_L} \sqrt{\frac{8}{\pi M RT}}\, \frac{Q_L^V}{Q_G^{Kn}} \quad \text{(Eq. VI.29)}$$

$$\frac{\left(Q_G^{Kn}\right)^2}{Q_L^V\, Q_m^D} = \frac{256\, \mu_L}{9\, \pi\, M\, RT\, \rho_L\, D_\infty} \quad [\text{mol m}^{-3}\ \text{s}^{-1}\ \text{Pa}^{-1}] \quad \text{(Eq. VI.30)}$$

VI.1.3. Characterization of PSDs in porous asymmetric membranes

VI.1.3.1. Contribution of the support

The contribution of the support has been omitted in our preliminary considerations in section VI.1.2. Nevertheless, for asymmetric membranes with meso- or macroporous active layers (such of UF and NF membranes), the permeation behavior can be strongly influenced by the porous nature of the support. Therefore, prior to the determination of the mean diameters for the further determination of log-normal PSDs of the active layers, the contribution of the support must be removed from the overall permeance for each permeation experiment. The overall permeance that includes the contribution of both the top layer and the support can be expressed by Eqs. VI.31

$$\frac{1}{Q_i^T} = \frac{1}{Q_{i,M}^T} + \frac{1}{Q_{i,S}^T}, \quad \text{(Eq. VI.31)}$$

where the subscript **i** refers to the gas (**i = G**), liquid (**i = L**) and non-hindered diffusion of an electrolyte (**i = m**), while the subscripts **M** and **S** refer, respectively, to the permeances related to the active layer and to the support. Under the assumption that the support can be characterized by a narrow unimodal PSD that approaches a δ-Dirac function, which seems

reasonable for commercial membranes, the latter permeances can be computed by the set of Eqs. VI.32-VI.34

$$Q^{T}_{G,S} = Q^{Kn}_{G,S} + Q^{V}_{G,S} = \frac{1}{3}\sqrt{\frac{8}{\pi M R T}}\frac{1}{R_{S,1}} + \frac{P_m}{32\mu_G R T}\frac{1}{R_{S,2}} \quad [\text{mol m}^{-2}\ \text{s}^{-1}\ \text{Pa}^{-1}] \quad \text{(Eq. VI.32)}$$

$$Q^{T}_{L,S} = Q^{V}_{L,S} = \frac{\rho_L}{32\, M\, \mu_L}\frac{1}{R_{S,2}} \quad [\text{mol m}^{-2}\ \text{s}^{-1}\ \text{Pa}^{-1}] \quad \text{(Eq. VI.33)}$$

$$Q^{T}_{m,S} = Q^{D}_{m,S} = \frac{D_{\pm}}{R_{S,0}} \quad [\text{m s}^{-1}], \quad \text{(Eq. VI.34)}$$

$$\text{for } R_{S,i} = \frac{\tau_S\, \ell_S}{\varepsilon_S\, \bar{d}^{\,i}_S} \quad [\text{m}^{(1-i)}], \quad \text{(Eq. VI.35)}$$

where $\boldsymbol{\varepsilon_S}$, $\boldsymbol{\tau_S}$ and $\boldsymbol{\ell_S}$ are, respectively, the porosity [-], tortuosity [-] and thickness of the support [m], and $\mathbf{D_{\pm}}$ is the diffusivity of the electrolyte [$m^2\ s^{-1}$]. It should be noted that, for a single-gas permeance experiment, although the active top layer behaves according to a pure Knudsen diffusion mechanism, the support can show contribution of the viscous mechanism (see Eq. VI.32) on the grounds of the higher mean pore size of the latter.

Furthermore, it should be also highlighted that the contribution of the support to the overall mass transfer through a composite membrane is strongly dependent on the moment of the PSD of the active layer that governs the permeation mechanism. Table VI.1 shows some preliminary calculations performed for a model asymmetric membrane with δ-Dirac PSDs in both the active layer and support and with relevant parameters similar to those that can be found in commercial UF, NF and MF ceramic membranes (<u>active layer</u>: $\varepsilon_M / \tau_M = 0.05$ [-], ℓ_M =50 μm, $\bar{d}_M$ = 20 nm; <u>support</u>: $\varepsilon_S / \tau_S = 0.16$ [-], ℓ_S =2 mm, $\bar{d}_S$ = 2 μm). As can be seen, the lower the moment of the PSD that governs the permeation process, the higher the contribution of the support to the overall mass transfer. In this way, the non-hindered electrolyte diffusion through an asymmetric membrane tends to be more influenced by the support (contribution up to 99%) than the permeation of a pure liquid governed by a pressure-driven viscous mechanism, where the active layer governs the permeation behavior.

In view of these observations and to the dependence of the diffusive flux with the moments of the PSD according to Eq. VI.18, both the hindered and non-hindered diffusive permeation of a species through a porous asymmetric membrane tends to be governed by the support. Accordingly, in practice, the diffusion of a species across an asymmetric membrane does not provide relevant structural information concerning the active layer. Nevertheless, it constitutes a good tool for the characterization of the support in terms of the ratio $\boldsymbol{\tau_S\, \ell_S/\varepsilon_S}$ or resistance $\mathbf{R_{S,0}}$.

Table VI.1: Contribution of the support to the overall mass transfer for single-gas permeance, pure liquid permeability and non-hindered electrolyte diffusion experiments for a δ-Dirac PSD in the active layer. Input data for the active layer: ε_M / τ_M = 0.05 [-], ℓ_S = 50 μm, $\overline{d}_M$ = 20 nm. Input data for the support: ε_S / τ_S = 0.16 [-], ℓ_S = 2.5 mm, $\overline{d}_S$ = 2 μm.

Experiment	*i [-]*	*Active layer*	*Support*	$\frac{R_{S,i}}{R_{M,i}+R_{S,i}}$ *[%]*
Pure liquid permeability	2	$R_{M,2} = \frac{\tau_M \ell_M}{\varepsilon_M \overline{d}_M^2}$	$R_{S,2} = \frac{\tau_S \ell_S}{\varepsilon_S \overline{d}_S^2}$	**0.4%**
Single-gas permeance (N_2)	1	$R_{M,1} = \frac{\tau_M \ell_M}{\varepsilon_M \overline{d}_M}$	$R_{S,1} = \frac{\tau_S \ell_S}{\varepsilon_S \overline{d}_S}$	**28.1%**
Non-hindered electrolyte diffusion	0	$R_{M,2} = \frac{\tau_M \ell_M}{\varepsilon_M}$	$R_{S,0} = \frac{\tau_S \ell_S}{\varepsilon_S}$	**97.5%**

VI.1.3.2. Determination of experimental overall permeances

This section deals with the determination of single-gas, pure liquid and electrolyte non-hindered diffusion permeances through NF and MF asymmetric membranes. The former two permeances allow the determination of diameter $\overline{d}_2$ of the PSD of the active layer, $\overline{d}_{M,2}$ in the reminder of this chapter, while the latter allows the determination of the ratio $\tau_S \ell_S/\varepsilon_S$ of the support. The details concerning the experimental setup and procedures used for the experimental determination of all three permeances can be found in section III.2.2. Table VI.2 summarizes the results obtained for these permeances for a set of commercial inner-side tubular TiO_2 (rutile) NF and MF membranes. The calculations involved in the determination of these three permeances from experimental data constitute the subject of discussion in the forthcoming sections (VI.3.2.1 – VI.3.2.3).

VI.1.3.2.1. Single-gas permeance experiments

The relationship between the permeate pressure and time is given by a mass balance equation in the permeate volume (Eq. VI.36)

$$\frac{dn_2}{dt} = \frac{V_2}{RT}\frac{\delta P_2(t)}{\delta t} = Q_G^T S_{in}\left[P_1 - P_2(t)\right] \text{ [mol s}^{-1}\text{]}, \qquad \text{(Eq. VI.36)}$$

where S_{in} is the geometrical area of the inner surface of the membrane tube [m^2], P_1 is the feed pressure [kPa], which was kept at a constant value for each experiment, and P_2 is the permeate pressure [kPa]. Eq. VI.36 can be solved analytically using the initial condition (Eq. VI.37)

Table VI.2: Commercial inner-side tubular asymmetric TiO_2 membranes used in this study

Membrane *	*MWCO [kD]*	*No. of internal holes*	*S_{in} [cm^2]*	*Q^T_G x10^6 (1) [mol m^{-2} s^{-1} Pa^{-1}]*	*Q^T_L x10^{11} (2) [m^3 m^{-2} s^{-1} Pa^{-1}]*	*Q^T_{HCl} x10^7 (3) [m s^{-1}]*
1	1	3	95.2	4.34 ± 0.13	2.96 ± 0.02	2.61 ± 0.48
2	1	3	95.2	-	-	2.15 ± 0.84
3	8	3	95.2	6.60 ± 0.07	20.2 ± 0.1	2.04 ± 0.10
4	50	3	95.2	6.60 ± 0.08	58.1 ± 0.07	1.98 ± 0.09
5	150	3	95.2	6.75 ± 0.09	106 ± 3	2.05 ± 0.06
6	0.14 μm	3	95.2	-	417	-
7	0.20 μm	3	95.2	-	528	-
8	0.45 μm	3	95.2	8.11 ± 0.30	722 ± 2	2.65 ± 0.04
9	0.80 μm	3	95.2	-	764	-
10	0.80 μm	1	51.5	9.41	817 ± 5	4.07 ± 0.09

Temperature: (1) 301 – 303 K
(2) 288 – 298 K
(3) 298 – 299 K

$$t = 0 \;\rightarrow\; P_2 = P_2(0) \qquad \text{(Eq. VI.37)}$$

Furthermore, the overall gas permeance that includes the contribution of both the top layer and the support is given by Eq. VI.38

$$\frac{1}{Q_G^T} = \frac{1}{Q_{G,M}^{Kn}} + \frac{1}{Q_{G,S}^{Kn} + Q_{G,S}^{V}} = \frac{R_{M,1}}{Q_{G,1}} + \frac{1}{Q_{G,1}} \frac{1}{\frac{1}{R_{S,1}} + \frac{Q_{G,2}}{R_{S,2}}\left(P_2^S + P_2\right)}, \qquad \text{(Eq. VI.38)}$$

where $\mathbf{P_2^S}$ is the pressure at the active layer / support surface [kPa]. This pressure can be calculated by Eq. VI.39

$$P_2^S = \frac{-\left(R_{M,1} + R_{S,1}\right) + \sqrt{\left(R_{M,1} + R_{S,1}\right)^2 + 4\,\bar{d}_S\, R_{M,1}\left(R_{S,1}\, P_1 + R_{M,1}\, P_2 + \bar{d}_S\, Q_{G,2}\, R_{M,1}\, P_2^2\right)}}{2\,\bar{d}_S\, Q_{G,2}\, R_{M,1}}$$

(Eq. VI.39)

where $R_{G,M}$ and $R_{G,S}$ are defined, respectively, by Eqs. VI.23 and VI.35, while $Q_{G,1}$ and $Q_{G,2}$ are defined, respectively, by Eqs. VI.40 and VI.41

$$Q_{G,1} = \frac{1}{3}\sqrt{\frac{8}{\pi M RT}} \qquad \text{(Eq. VI.40)}$$

$$Q_{G,2} = \frac{\frac{1}{\sqrt{64\,\mu_G\,RT}}}{\frac{1}{3}\sqrt{\frac{8}{\pi\,M\,RT}}} = \frac{3}{64\,\mu_G}\sqrt{\frac{\pi\,M}{8\,RT}} \qquad \text{(Eq. VI.41)}$$

Introducing Eqs. VI.39-VI.41, VI.23 and VI.35 into Eq. VI.38, for permeate pressures $P_2 < 0.60\,P_1$, Eq. VI.42 is obtained for the overall single-gas permeance, Q_G^T

$$Q_G^T = \frac{Q_{G,1}}{R_{M,1} + Q_{G,2}\left[\frac{-\left(R_{M,1}+R_{S,1}\right)+\sqrt{\left(R_{M,1}+R_{S,1}\right)^2+4\,\bar{d}_S\,R_{M,1}\,R_{S,1}\,P_1}}{2\,\bar{d}_S\,Q_{G,2}\,R_{M,1}}\right]\bar{d}_S + 1}$$

(Eq. VI.42)

which is independent of P_2. $R_{M,1}$ can be calculated by isolating it from Eq. VI.42

$$R_{M,1} = \frac{Q_{G,1} + 2\,\bar{d}_S\,Q_{G,1}\,Q_{G,2}\,P_1 - \sqrt{Q_{G,1}}\sqrt{4\,\bar{d}_S\,Q_G^T\,Q_{G,2}\,R_{S,1}\,P_1 + Q_{G,1}}}{2\,\bar{d}_S\,Q_G^T\,Q_{G,2}\,P_1} \qquad \text{(Eq. VI.43)}$$

Finally, it should be noted that, on the grounds of its independence of P_2, the overall single-gas permeance can be experimentally determined by integrating Eq. VI.36 for the initial condition Eq. VI.37

$$\mathrm{Ln}\left[\frac{P_1 - P_2(t)}{P_1 - P_2(0)}\right] = -\frac{S_{in}}{V_2}\,RT\,Q_G^T\,t \qquad \text{(Eq. VI.44)}$$

As an example, Figure VI.2 plots $\mathrm{Ln}[(P_1 - P_2)/(P_1 - P_2\,(0))]$ vs. time for an experiment performed with N_2 for UF membrane 1 (1 kD) according to Table VI.2.

VI.1.3.2.2. Pure liquid permeability experiment

The permeability of liquid water for a given membrane can be calculated as the quotient of the water flux, $\mathbf{N_w}$ [L m^{-2} h^{-1}], by the applied transmembrane pressure, $\mathbf{\Delta P}$ [bar] (Eq. VI.45)

$$Q_L^T = \frac{N_w}{\Delta P} \quad [m^3\ m^{-2}\ s^{-1}\ Pa^{-1}] \qquad \text{(Eq. VI.45)}$$

Furthermore, to elucidate the contribution of the support, some preliminary water permeability tests were performed on a set of asymmetric MF membranes (see Table VI.2). Assuming that the PSD of the active layer is very narrow, the resistance $R_{S,2}$ of the support can be calculated from the intercept of the linear representation of the inverse of water

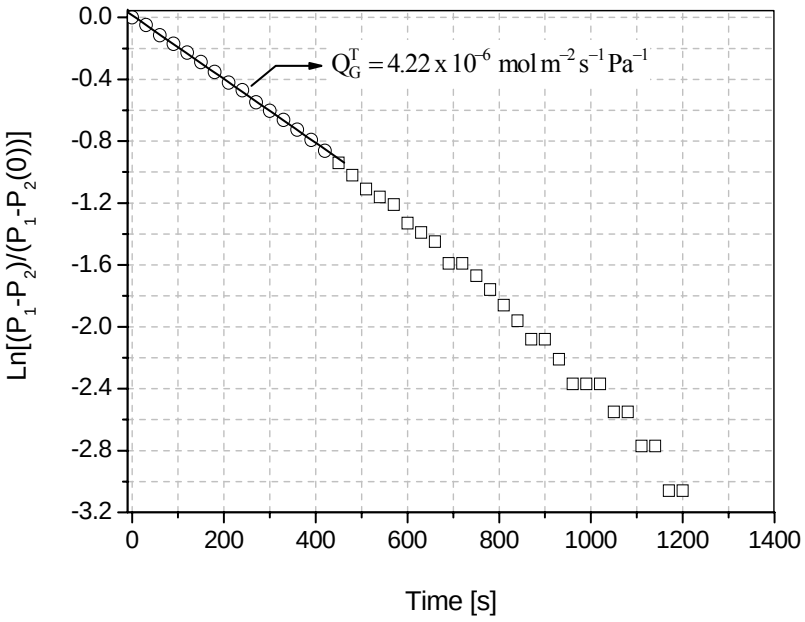

Figure VI.2: Plot of Ln[$(P_1 - P_2)/(P_1 - P_2(0))$] vs. time for the single-gas permeance of N_2 through membrane 1 (1 kD). The straight line refers to the linear fitting.

permeability with the inverse of the square mean pore size of the active layer (Eq. VI.46), while the resistance $R_{M,0}$ of the active layer can be calculated from the slope of this representation

$$\frac{1}{Q_L^T} = \frac{\tau_M \ell_M}{\varepsilon_M} \frac{32\mu_L}{\bar{d}_M^2} + \frac{\tau_S \ell_S}{\varepsilon_S} \frac{32\mu_L}{\bar{d}_S^2} = 32\mu_L \left(\frac{R_{M,0}}{\bar{d}_M^2} + R_{S,2} \right) \text{ [Pa s m}^2 \text{ m}^{-3}\text{]} \quad \text{(Eq. VI.46)}$$

According to the linear fitting plotted in Figure VI.3, the values of the resistances $\mathbf{R_{M,0} = 6.94 \times 10^{-5}\ m}$ and $\mathbf{R_{S,2} = 4.03 \times 10^{9}\ m^{-1}}$ can be estimated for both the active layers and the support. Since all the membranes 1-9 were provided by the same manufacturer and the active layers were grown on the same kind of support, the resistance $R_{S,2}$ related to the support is expected to describe the permeation behavior of the support for all the membranes 1-9. Therefore, this value was used to characterize the support for all the membranes 1-9 listed in Table VI.2. However, the resistance $R_{M,0}$ related to the active layer is in principle only applicable to membranes 6-9, since the characteristics of the active layers deposited onto the supports are strongly dependent on their mean pore size and can differ from those of UF and MF membranes 1-5.

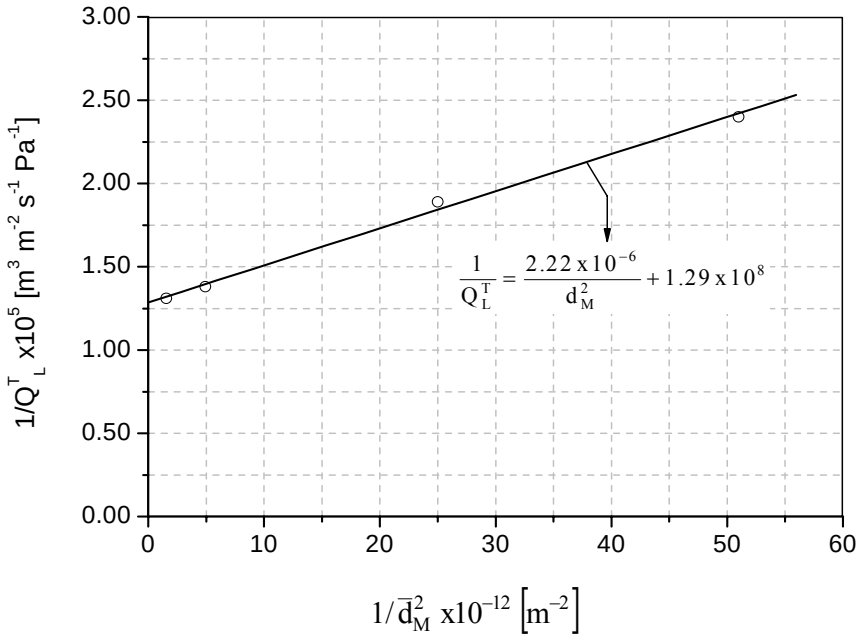

Figure VI.3: Plot of $1/Q^T_L$ vs. $1/\bar{d}^2_M$ for water permeability experiments for commercial TiO_2 asymmetric MF membranes 6-9 (see Table VI.2). The straight line refers to the linear fitting.

VI.1.3.2.3. Non-hindered electrolyte diffusion experiments

The relationship between the concentration of a target ion in the permeate volume and time is given by a mass balance equation in the permeate volume (Eq. VI.47) and application of the Fick's first law

$$\frac{dn_2}{dt} = V_2 \frac{\delta C_2(t)}{\delta t} = Q^D_{m,T} S_{in} \left[C_1(t) - C_2(t)\right] \text{ [mol s}^{-1}\text{]}, \qquad \text{(Eq. VI.47)}$$

where S_{in} is the geometrical area of the inner surface of the membrane [m^2] in contact with the feed solution and $C_1(t)$ and $C_2(t)$ is the concentration of the electrolyte in the feed and permeate volumes, respectively. Eq. VI.47 can be integrated using the following initial condition (Eq. VI.48)

$$t = 0 \rightarrow C_1(t) = C_1(0),\ C_2(t) = C_2(0) \qquad \text{(Eq. VI.48)}$$

and a mass balance equation of the electrolyte (Eq. VI.49)

$$V_1 C_1(0) + V_2 C_2(0) = V_1 C_1(t) + V_2 C_2(t), \qquad \text{(Eq. VI.49)}$$

thus giving Eq. VI.50

$$\mathrm{Ln}\left[\frac{C_1(0)+\frac{V_2}{V_1}C_2(0)-\left(1+\frac{V_2}{V_1}\right)C_2(t)}{C_1(0)\ -C_2(0)}\right]=-Q^{D}_{m,T}\,S_{in}\left(\frac{1}{V_1}+\frac{1}{V_2}\right)t \qquad \text{(Eq. VI.50)}$$

which can be simplified to Eq. VI.51 if $V_1 >> V_2$

$$\mathrm{Ln}\left[\frac{C_1(0)-C_2(t)}{C_1(0)-C_2(0)}\right]=-\frac{S_{in}}{V_2}\,Q^{D}_{m,T}\,t \qquad \text{(Eq. VI.51)}$$

For practical purposes, Eq. VI.50 can be rewritten to Eq. VI.52 through the definition of parameter $\Psi = \{[C_1(0)+(V_2/V_1)\,C_2(0)-(1+V_2/V_1)\,C_2(0)]/[C_1(0)-C_2(0)]\}$

$$\mathrm{Ln}(\Psi)=-Q^{D}_{m,T}\,S_{in}\left(\frac{1}{V_1}+\frac{1}{V_2}\right)t \qquad \text{(Eq. VI.52)}$$

As an example, Figure VI.4 plots the representation of $\mathrm{Ln}(\Psi)$ vs. time for an experiment performed with N_2 for UF membrane 1 (1 kD) according to Table VI.2.

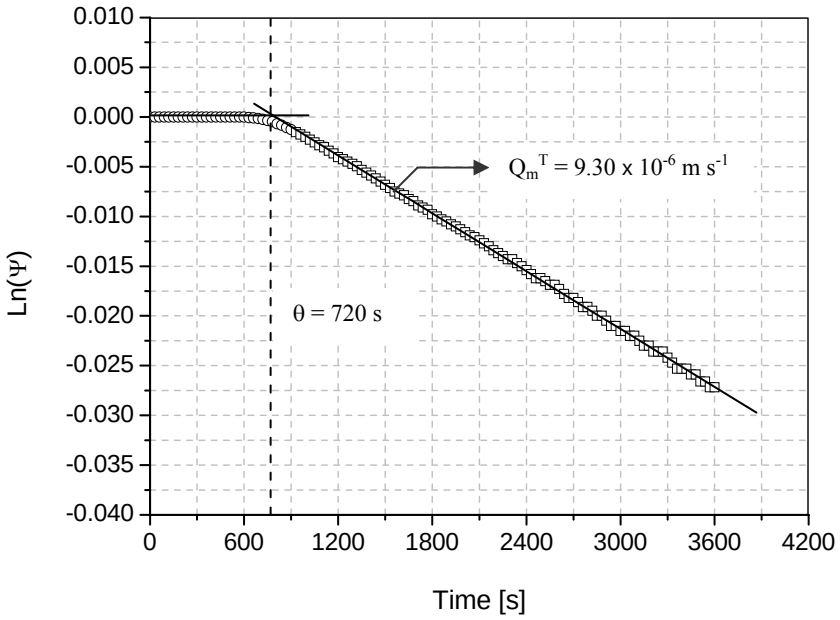

Figure VI.4: Plot of Ln(Ψ) vs. time for the diffusion of H^+ (HCl) through membrane 1 (1 kD), keeping both the feed and permeate solutions at I = 500 mM. The time lag (θ) for this experiment was 720 s.

Moreover, the thickness of the support, ℓ_S, can be also experimentally determined from the resistance $R_{S,0}$ of the support and the ***time lag***, θ [s], that is, the delay observed in the reception of the signal in the permeate volume. For plane sheet geometries, Eq. VI.53 is proposed (*Crank, 2004*)

$$\theta = \frac{\tau_S \, \ell_S^2}{6 \, D_\pm \, \varepsilon_S} = \frac{R_{S,0} \, \ell_S}{6 \, D_\pm} \text{ [s]} \quad \rightarrow \quad \ell_S = \frac{6 \, D_\pm \, \theta}{R_{S,0}} \text{ [m]} \qquad \text{(Eq. VI.53)}$$

The thickness of the support allows to calculate the $R_{S,0}$ ratio of the support by Eq. VI.54

$$\frac{\varepsilon_S}{\tau_S} = \frac{\ell_S}{R_{S,0}} \left(\text{No. of holes} \right) \qquad \text{(Eq. VI.54)}$$

On the other hand, the knowledge of resistance $R_{S,0}$ and $R_{S,2}$ of the support, the latter determined from Eq. VI.46, allows the determination of the mean pore size of the support, $\bar{d}_S$ [m], through the use of Eq. VI.54, which in its turn allows the calculation of the resistance $R_{S,1}$ of the support

$$\bar{d}_S = \sqrt{\frac{R_{S,0}}{R_{S,2}}} \text{ [m]} \quad \rightarrow \quad R_{S,1} = R_{S,2} \, \bar{d}_S \text{ [-]} \qquad \text{(Eq. VI.55)}$$

Great care was taken in all the experiments to avoid any effect of the ζ-potential on the pore walls both in the active layers and supports in the electrolyte diffusion. To this end, several experiments were performed at the same conditions, but changing the ionic strength, **I** [mM], at both the permeate and retentate volumes of the experimental set-up (see Figure III.16). Figure VI.5 plots the trend observed for the fitted values of $R_{S,0}$ with the ionic strength for membrane 2 (1 kD). As can be seen, the fitted values of $R_{S,0}$ tend to decrease with the ionic strength until a stable value ~2.40×10^{-2} m beyond 500 mM. In light of this trend, all the non-hindered electrolyte diffusion experiments were carried out at I = 500 mM. Furthermore, to assess that the results did not depend on the permeating electrolyte, some additional experiments were done with membrane 2 for the diffusion of LiOH and KOH instead of HCl, keeping the ionic strength at 500 mM, respectively, with LiCl and KCl, which revealed no dependence of the permeation behavior on the diffusing species.

VI.1.3.3. Membrane characterization in terms of mean diameter $\bar{d}_{M,2}$ and ε_S/τ_S

Figure VI.6 shows the schematic representation of the procedure used for the determination of mean diameters $\bar{d}_{M,2}$ of the active layers and ε_S / τ_S ratios of the supports for the set of commercial asymmetric membranes listed in Table VI.2. In general terms, the calculation strategy consists of two steps: (1) Determination of the resistances $R_{S,0}$, $R_{S,1}$ and

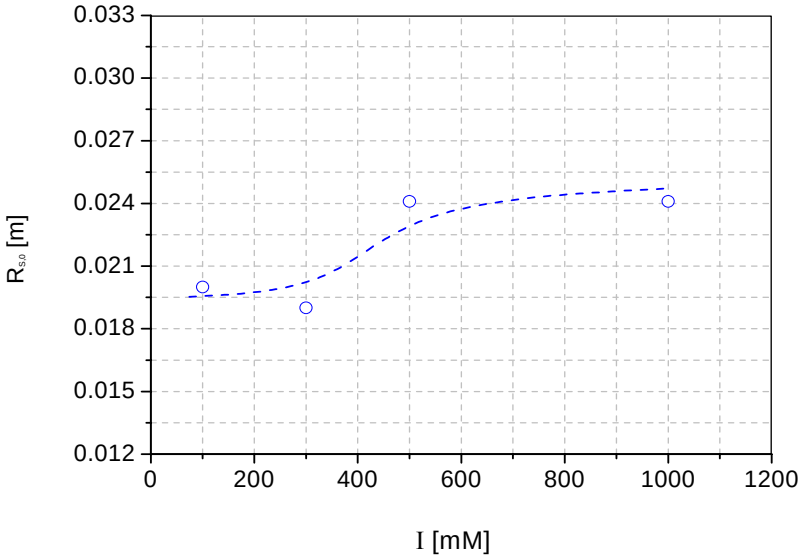

Figure VI.5: Evolution of fitted values of $R_{S,0}$ with the ionic strength (KCl) for HCl non-hindered diffusion through membrane 2 (1 kD). The dashed line refers to the trend observed.

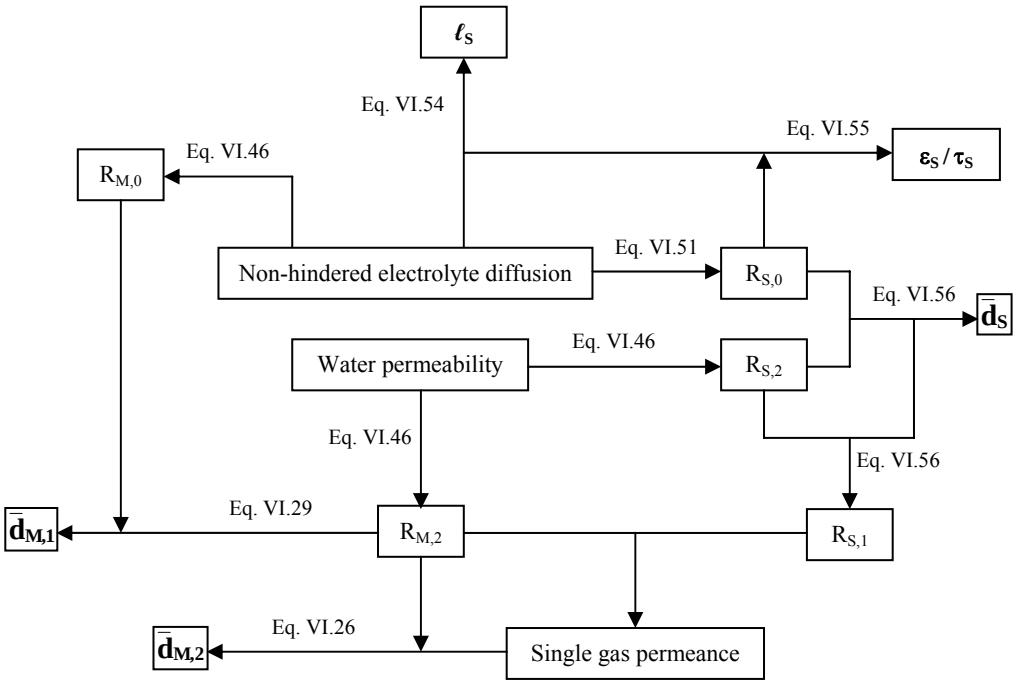

Figure VI.6: Schematic representation of the procedure used for the determination of mean diameters $\mathbf{d_{M,2}}$ and $\boldsymbol{\varepsilon_S / \tau_S}$ ratios for the characterization of the NF and MF asymmetric membranes listed in Table VI.2.

$\mathbf{R_{S,2}}$ related to the support, and (2) determination of the resistances $\mathbf{R_{M,1}}$ and $\mathbf{R_{M,2}}$ related to the active top layer. Subsequently, $\boldsymbol{\varepsilon_S / \tau_S}$ ratios can be directly calculated using Eq. VI.54, while mean diameters $\bar{d}_{M,2}$ can be calculated using Eq. VI.26. The results obtained for some of the membranes listed in Table VI.2 are summarized in Table VI.3. As can be seen, as would be expected, the membranes with higher MWCO or mean pore sizes show higher computed $\bar{d}_{M,2}$ mean diameters. Moreover, Figure VI.7 shows a linear trend in double logarithmic axes between the MWCO and $\bar{d}_{M,2}$ mean diameters for the former membranes.

Table VI.3: Commercial tubular asymmetric TiO_2 membranes used in this study

Membrane *	*MWCO [kD]*	$R_{M,2}$ (1) *x10^{-8} [m^{-1}]*	$R_{M,1}$ (2) *x10^{-3} [-]*	$R_{S,0}$ (3,4) *x10^{-2} [m^{1}]*	$\bar{d}_{M,2}$ *[nm]*	ε_S/τ_S *[-]*
1	1	11772 ± 65	7.07 ± 0.97	1.91 ± 0.10	6.0 ± 0.8	0.16 ± 0.09
3	8	1519 ± 7	1.83 ± 0.11	2.52 ± 0.13	12.0 ± 0.8	0.12 ± 0.01
4	50	492 ± 6	1.82 ± 0.11	2.59 ± 0.12	37.0 ± 2.3	0.12 ± 0.01
5	150	311 ± 1	1.65 ± 0.13	2.50 ± 0.05	52.4 ± 3.3	0.12 ± 0.03
8	0.45 µm	4.72 ± 0.10	0.21 ± 0.01	2.10 ± 0.07	454 ± 27 (5)	0.15 ± 0.02
10	0.80 µm	3.40 ± 0.21	1.33 ± 0.01	1.27 ± 0.01	875 ± 42	0.16 ± 0.01

* Support: $R_{S,2} = 4.03 \times 10^{9}$ m^{-1} for membranes 1-5 ($\bar{d}_S = 2.3$ µm for membranes 1-9)
$R_{S,2} = 3.13 \times 10^{9}$ m^{-1} for membranes 6 ($\bar{d}_S = 2.0$ µm for membrane 10)

(1) Determined from pure water permeability experiments

(2) Determined from N_2 permeance experiments

(3) Determined from the non-hindered diffusion of HCl (I = 500 mM). $D_{HCl} = 5.14 \times 10^{-9}$ m^2 s^{-1} (*Weast, 1998*)

(4) Time lag: θ = 650-780 s for membranes 1-8 and 480-600 s for membrane 10

(5) $R_{M,0} = 6.94 \times 10^{-5}$ m calculated from Figure VI.3 (Eq. VI.46) → computed $\bar{d}_{M,1} = 324 \pm 20$ nm

It should be emphasized that diameters $\bar{d}_{M,1}$ might be also calculated if the resistance $\mathbf{R_{M,0}}$ is known. Unfortunately, as was aforementioned in sections VI.1.1.3.2.2 and VI.1.3.2.3, no significant data could be obtained for this resistance from water permeability and non-hindered electrolyte diffusion experiments. However, for membrane 8 (theoretical mean pore size = 0.45 µm), this resistance could be estimated from the intercept of Eq. VI.46 (see Figure VI.3), which was used in the present study to provide a rough estimation of the ε(d) of the PSD of this membrane (see Figure VI.8).

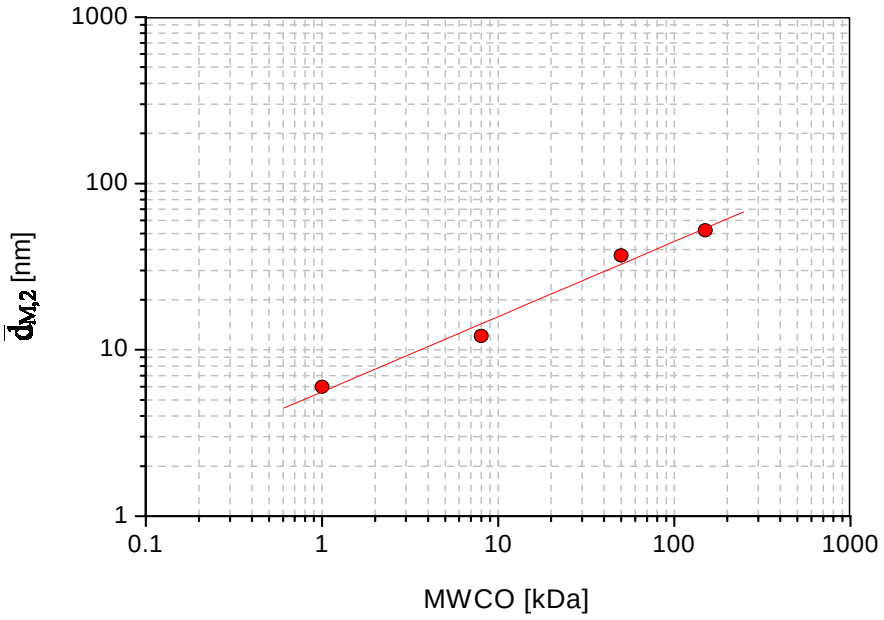

Figure VI.7: Evolution of computed $\bar{d}_{M,2}$ diameters with the MWCO for membranes 1, 3, 4 and 5 (see Table VI.3). The straight line refers to the trend observed.

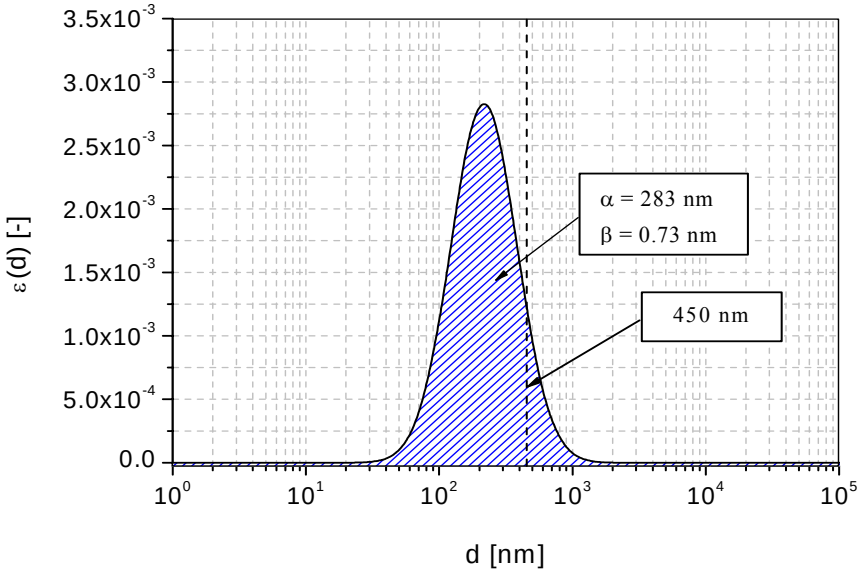

Figure VI.8: Normalized log-normal density function ε (d) computed from mean diameters $\bar{d}_{M,1}$ = 324 ± 20 nm and $d_{M,2}$ = 454 ± 27 nm calculated from experimental permeation data for membrane 8 (theoretical mean pore size = 450 nm) (see Table VI.3)

VI.2. CHARACTERIZATION OF INTERCRYSTALLINE LARGE DEFECTS IN ZEOLITE NaA MEMBRANES FROM VPV MEASUREMENTS

The general concepts put forward in section VI.1 for the determination of PSDs in porous asymmetric membranes are reconsidered in this section for the characterization of large defects (either meso- and macropores, fissures or cracks) in composite zeolite NaA membranes from VPV data. As was discussed in section IV.5, although a zeolite NaA membrane shows good selectivity towards the dehydration of ethanol/water mixtures, the presence of a certain number of large pores in the zeolite layers cannot be ruled out.

In general terms, a zeolite NaA membrane is visualized as a system where a liquid mixture is put in contact with a zeolite thin layer grown onto a much thicker porous support. If both the feed (retentate) and the permeate volumes are considered to be well-mixed, mass transfer must be wholly ascribed to the membrane (zeolite layer + support). Furthermore, according to *Nomura et al. (2001)*, on the grounds of its polycrystalline nature, the zeolite layer is viewed as an assembly of zeolite grains (see Figure VI.9) that might include two kinds of pores: (1) ***intracrystalline*** or ***zeolite pores***, and (2) ***intercrystalline*** or ***non-zeolite pores***. The former consist of subnanometric pores (mean pore size <1 nm) defined by the zeolitic crystalline lattice, while the latter might include grain boundaries in the borderline between adjacent zeolite single crystals, low intergrown regions, and large meso-and macropores or cracks in the zeolite layer due to, for instance, an inefficient synthesis process or due to thermal stress during the operation of the membrane. Intra- and intercrystalline pores might involve different pathways for mass transfer due to their different nature. Among intercrystalline pores, grain boundaries are usually regarded as a special kind of micropores, because they have pore sizes <1 nm. Both intracrystalline and grain boundaries are responsible for the high selectivities that zeolite membranes show towards the separation of different species on the basis of adsorption and surface diffusion differences.

Nevertheless, if a number of intercrystalline large pores or low intergrown regions are present in the zeolite layer (i.e. the membrane is not defect-free), the membrane will lose partially its separation ability depending on the number of large pores and on their characteristics, because they are not able to distinguish between molecules of different sizes or physicochemical properties (in the remainder of this work, the term “intercrystalline porosity” will be used to account for the porosity related to large pores in a zeolite layer).

Most of the studies reported in the literature concern the characterization of intercrystalline porosity by gas permeance measurements in MFI type membranes (e.g., *Sanchez et al., 2001; and Hanebuth et al., 2005*). This section is intended to show that relevant data concerning large pores can be also obtained from VPV experiments. An application is illustrated for several zeolite NaA membranes prepared in our laboratory.

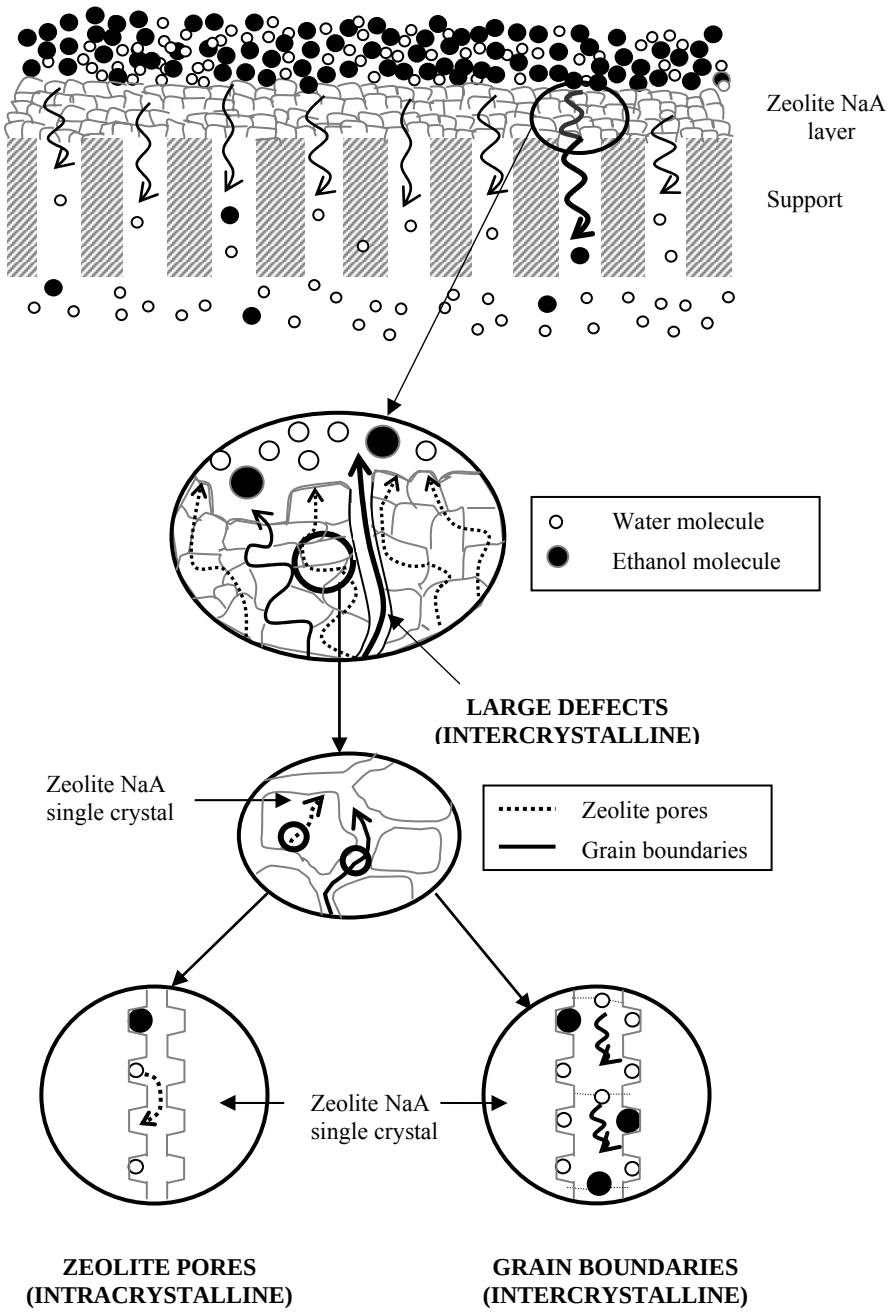

Figure VI.9: Schematic representation of the intracrystalline and intercrystalline pathways for mass transfer in the zeolite layer.

VI.2.1. Modeling

In analogy with the ideas put forward in section VI.1, large pores in a zeolite NaA layer are regarded as cylindrical and straight ($\tau = 1$) capillaries. In the VPV process through large pores, the molecules in the liquid feed might be transferred to the vapor permeate side of the membrane by three main mechanisms: Knudsen diffusion, pressure-driven viscous flux and surface diffusion. For practical purposes, assuming that the PSD of large defects can be defined by a narrow unimodal function, namely, all the pores are identical, the former two mechanisms, Knudsen diffusion and pressure-driven viscous flux, can be described, respectively, by Eqs. VI.6 and VI.7. Moreover, surface diffusion implies the diffusion of adsorbed molecules on the pore wall by skating across the surface to reach the other side. Because this latter mechanism is hard to confirm directly, it is usually inferred by comparing the flux observed with that expected from measurements with helium, which is believed never to undergo surface transport.

An important point in the present description is to describe how the liquid feed evaporates before reaching the vapor permeate. Figure VI.10 illustrates the process. Because the mean pore size of the support used in the synthesis of zeolite NaA membranes is regarded to be much higher than that of defects in the zeolite layer (see Table III.1), the evaporation of the liquid is assumed to take place at position **C** within the latter at a certain distance, $\mathbf{z_L}$ [m], comprised between the liquid feed and the zeolite layer – support surface (**S**) (see Figure VI.10) in the similar manner as that proposed by *Abeles et al. (1991)* for modeling capillary condensation. Moreover, the pressure at which the liquid evaporates, $\mathbf{P_v^C}$ [kPa], differs from the saturation vapor pressure in the bulk, P^o [kPa], due to capillary forces according to the Kelvin equation (Eq. VI.56)

$$P_v^C = P^o \exp\left(-\frac{4\,\overline{M}\,\sigma}{\rho_L\,RT\,\overline{d}_C}\cos\theta\right), \qquad \text{(Eq. VI.56)}$$

where σ is the surface tension [N m^{-1}], ρ_L is the liquid density [kg m^{-3}], $\overline{d}_C$ is the mean pore size of the capillary [m], and θ the contact angle between the liquid and the pore wall [º]. If the liquid wets the pore, $\theta < 90^o$ and $P_v^C < P^o$, the equilibrium vapor pressure in the pore is reduced below the saturation pressure. It should be noted that Eq. VI.56 is only valid for a pure species and for $\overline{d}_C$>2 nm. For multicomponent systems, modified versions of the Kelvin equation can be found in the literature (*Shapiro and Stenby, 1997*).

Furthermore, at interfacial equilibrium, a meniscus might be formed at position C due to capillary forces, which implies that the total pressure of the liquid and vapor at this position, $\mathbf{P_v^C}$ and $\mathbf{P_L^C}$, respectively, differ according to the Young-Laplace equation (Eq. VI.57)

$$P_L^C = P_v^C - \frac{4\sigma}{\bar{d}_C}\cos(\theta) \quad [\text{kPa}] \qquad \text{(Eq. VI.57)}$$

In fact, the vapor side of the meniscus is regarded to lie under a non-equilibrium situation due to the sweeping action of vacuum, which might imply that the meniscus at position C tends to be flat (see Figure VI.10). For this particular situation, $P_v^C \rightarrow P^o$ and $P_L^C \rightarrow P_v^C$. Moreover, in case of a multicomponent mixture, the Raoult Law can be applied at position C to relate the

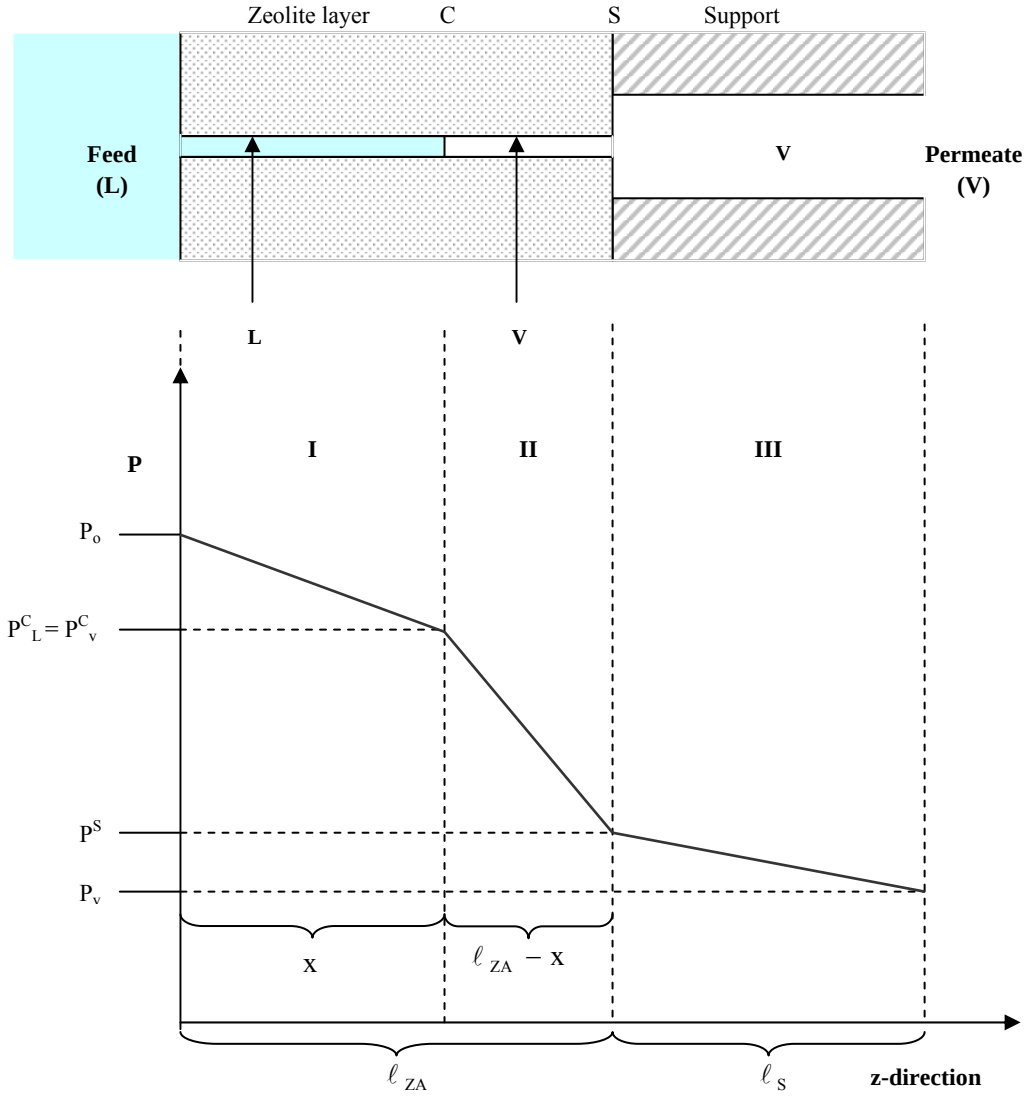

Figure VI.10: Pressure gradient in the thickness of a composite zeolite NaA membrane (zeolite layer + support). The pore partially fills with a liquid ($\theta = 90^o$) as shown by the shaded blue region that evaporates at position C. The zeolite layer and support thickness are not scaled.

compositions of each species **i** at the liquid and vapor sides, $\mathbf{x_i^C}$ and $\mathbf{y_i^C}$, respectively [-] (Eq. VI.58)

$$P_{v,i}^{C} = y_i^{C}\, P_v^{C} = a_i^{C}\, P_{v,i}^{o} \quad [\text{kPa}], \qquad \text{(Eq. VI.58)}$$

where $a_i^C = \gamma_i^C\,(x_i^C, T)\, x_i^C$ is the activity of species **i** at the liquid side at position C [-]. The activity coefficients, $\boldsymbol{\gamma_i^C}$ [-], can be calculated by the UNIFAC method. A next point in the present description involves the quantification of the overall mass transfer through the membrane, which includes the contributions of the partially liquid-filled volume in the capillaries (zone I), vapor volume in the capillaries (zone II) and the contribution of the macroporous support (zone III).

VI.2.1.1. Zone I: Liquid-filled volume in the capillary

The flux in the liquid-filled volume of the capillary, $\mathbf{N_I^V}$ [mol m^{-2} s^{-1}], can be modeled as a pressure-driven viscous flux of the liquid for a liquid phase (Eq. VI.59)

$$N_I^V = \left[\frac{\rho_L\, \varepsilon_{inter}\, \overline{d}_C^{\,2}}{32\, \overline{M}\, \mu_L}\right]\frac{\Delta P}{z_l} = \frac{D_L}{RT}\frac{\Delta P}{z_L} \quad [\text{mol m}^{-2}\,\text{s}^{-1}], \qquad \text{(Eq, VI.59)}$$

where $\boldsymbol{\mu_L}$ is the viscosity of the liquid [kg m^{-1} s^{-1}], respectively, $\overline{\mathbf{M}}$ is the mean molar weight of the liquid feed in zone I [kg mol^{-1}], $\boldsymbol{\varepsilon_{inter}}$ is the intercrystalline porosity [-], and $\mathbf{z_L}$ is the length of the capillary filled with liquid [m] (see Figure VI.10). The quantity in square brackets in Eq. VI.59 can be regarded as a "viscous diffusivity", $\mathbf{D_L}$ [m^2 s^{-1}], although it is due solely to convective flow, which is defined by Eq. VI.60

$$D_L = RT\left[\frac{\rho_L\, \varepsilon_{inter}\, \overline{d}_C^{\,2}}{32\, \overline{M}\, \mu_L}\right] \quad [\text{m}^2\,\text{s}^{-1}] \qquad \text{(Eq. VI.60)}$$

It should be noted that the application of bulk density to a liquid condensed in a capillary is well supported by *Morishige et al. (1998)* and *Tzevelekos et al. (1998)*. However, while the liquid viscosity in the pores is believed to be higher than the bulk viscosity due to the interaction between the monolayer adsorbed on the pore walls (*Debye and Cleland, 1959*), the correlation is significant only for small pores (2-3 nm) and is less than a factor of 2 according to *Abeles et al. (1991)*. Moreover, the pressure difference in zone I, $\boldsymbol{\Delta P}$ [kPa], for the special case of θ=90º at position C (flat interface) is given by Eq. VI.61

$$\Delta P = P_o - P_L^C = P_o - P_v^C \qquad \text{(Eq. VI.61)}$$

Moreover, because the viscous flux is non-selective ($x_i^C \rightarrow x_i$), where x_i is the molar fraction of species **i** at the liquid side of the membrane [-], the total pressure at position C, P_v^C,

can be approached to the vapor saturation pressure, P_v^o, at the temperature at which the experiments are carried out.

VI.2.1.2. Zone II: Vapor-filled volume in the capillary

The flux in the vapor filled portion of the capillaries, $\mathbf{N_{II}^{Kn}}$ [mol m^{-2} s^{-1}], can be assumed to take place by Knudsen diffusion if the condition $P_{v,i}^C \bar{d}_C \leq 0.01$ Pa m for each species **i** is fulfilled. For a multicomponent system, because Knudsen diffusion is a selective process, the total flux is modeled by Eq. VI.62

$$N_{II}^{Kn} = \sum_{i=1}^{N} \frac{\varepsilon_{inter}\,\bar{d}_C}{3RT}\sqrt{\frac{8RT}{\pi M_i}}\frac{\left(P_{v,i}^C - P_{v,i}^S\right)}{\left(\ell_{ZA} - z_L\right)} = \sum_{i=1}^{N} \frac{D_{Kn,i}}{RT}\frac{\left(P_{v,i}^C - P_{v,i}^S\right)}{\left(\ell_{ZA} - z_L\right)} \qquad \text{(Eq. VI.62)}$$

where $\boldsymbol{\ell_{ZA}}$ is the thickness of the zeolite layer [m] and $\mathbf{P_{v,i}^C}$ and $\mathbf{P_{v,i}^S}$ correspond, respectively, to the partial pressure of the species i at the liquid-vapor interface (C) and at the zeolite layer – support surface [kPa]. The Knudsen diffusivity, $\mathbf{D_{Kn,i}}$ [m^2 s^{-1}], of each species **i** zone II is accounted for by Eq. VI.63 (see Eq. VI.6)

$$D_{Kn,i} = \frac{\varepsilon_{inter}\,\bar{d}_C}{3RT}\sqrt{\frac{8RT}{\pi M_i}} \quad [m^2\ s^{-1}] \qquad \text{(Eq. VI.63)}$$

VI.2.1.3. Zone III: Contribution of the macroporous support

Because the permeate is kept under vacuum in the VPV experiments, mass transfer across the macropores of the support in zone III is also assumed to be by Knudsen diffusion as in zone II (the relation $P_v^C \bar{d}_S < 0.01$ Pa m is fulfilled for $\bar{d}_S < 2$ mm and $P^S{}_v < 10$ kPa) according to Eq. VI.64

$$N_{III}^{Kn} = \sum_{i=1}^{N} \frac{\varepsilon_S\,\bar{d}_S}{3\tau_S RT}\sqrt{\frac{8RT}{\pi M_i}}\frac{\left(P_{v,i}^S - P_{v,i}\right)}{\ell_S} = \sum_{i=1}^{N} \frac{D_{Kn,i}}{RT}\frac{\left(P_{v,i}^S - P_{v,i}\right)}{\ell_S} \quad [\text{mol } m^{-2}\ s^{-1}],$$

(Eq. VI.64)

where $\boldsymbol{\varepsilon_S}$, $\boldsymbol{\tau_S}$, $\boldsymbol{\ell_S}$ and $\mathbf{\bar{d}_S}$ are, respectively, the porosity [-], tortuosity [-], thickness [m] and mean pore size of the support [m].

VI.2.1.4. Equation for overall mass transfer

At steady state, the equalities $N_I^V = N_{II}^{Kn} = N_{III}^{Kn}$ must hold. Given the equality $N_I^V = N_{II}^{Kn}$, the unknown $\mathbf{z_L}$ can be determined by combining Eqs. VI.59 and VI.62

$$\frac{D_L}{RT}\frac{\Delta P}{z_L}=\sum_{i=1}^{N}\frac{D_{Kn,i}}{RT}\frac{\left(P_{v,i}^{C}-P_{v,i}^{S}\right)}{\left(\ell_{ZA}-z_L\right)} \qquad \text{(Eq. VI.65)}$$

$$\frac{z_L}{\ell_{ZA}}=\frac{D_L\left(P_o-P_v^C\right)}{D_L\left(P_o-P_v^C\right)+\sum_{i=1}^{N}D_{Kn,i}\left(P_{v,i}^{C}-P_{v,i}^{S}\right)} \quad [-] \qquad \text{(Eq. VI.66)}$$

Therefore,

$$N_I^V=N_{II}^{Kn}=\frac{1}{\ell_{ZA}}\left\{\frac{D_L}{RT}\left(P_o-P_v^C\right)+\sum_{i=1}^{N}\frac{D_{Kn,i}}{RT}\left(P_{v,i}^{C}-P_{v,i}^{S}\right)\right\} \qquad \text{(Eq. VI.67)}$$

The total flux measured in a VPV experiment includes the overall contribution of surface diffusion of adsorbed molecules, $\mathbf{N^S}$ [mol m^{-2} s^{-1}], which in its turn includes the contribution of (1) surface diffusion of molecules that skate across the surface of the capillaries to reach the other side and (2) surface diffusion across zeolite pores and grain boundaries. Although both contributions cannot be in principle distinguished, the latter is expected to govern the surface diffusion because of the higher number of zeolite pores and grain boundaries than defects in a zeolite layer. Therefore, the overall mass transfer in a VPV experiment is described by Eq. VI.68

$$N^T=N^S+\frac{1}{\ell_{ZA}}\left[\frac{D_L}{RT}\left(P_o-P_v^C\right)+\sum_{i=1}^{N}\frac{D_{Kn,i}}{RT}\left(P_{v,i}^{C}-P_{v,i}^{S}\right)\right] \qquad \text{(Eq. VI.68)}$$

The set of Eqs. VI.68 and VI.64 for the contribution of the macroporous support allow the characterization of large defects in a zeolite layer. For the particular case that the support does not exert any significant contribution to the overall mass transfer, that is $P_{v,i}^{S}\rightarrow P_{v,i}$, Eq. VI.68 turns into Eq. VI.69

$$N^T=N^S+\frac{1}{\ell_{ZA}}\left[\frac{D_L}{RT}\left(P_o-P_v^C\right)+\sum_{i=1}^{N}\frac{D_{Kn,i}}{RT}\left(P_{v,i}^{C}-P_{v,i}\right)\right] \qquad \text{(Eq. VI.69)}$$

Eq. VI.70 allows the determination of mean pore sizes and intercrystalline porosities by representing N^T vs. P_o, namely, the presence of large defects in a zeolite layers should in principle involve a change in the total flux measured in a VPV experiment. Furthermore, according to Eq. VI.69, this dependence would be linear with a slope, $\boldsymbol{\lambda}$ [mol m^{-2} s^{-1} Pa^{-2}], and intercept, $\boldsymbol{\varphi}$ [mol m^{-2} s^{-1} Pa^{-1}], described, respectively, by Eqs. VI.70 and VI.71

$$\lambda=\text{Slope}=\frac{\delta N^T}{\delta P_o}=\frac{D_L}{RT\,\ell_{ZA}}=\left(\frac{\rho_L}{32\,\overline{M}\,\mu_L}\right)\frac{\varepsilon_{inter}\,\overline{d}_C^{\,2}}{\ell_{ZA}} \qquad \text{(Eq. VI.70)}$$

$$\varphi = \text{Intercept} = N^S - \left(\frac{\rho_L}{32\,\overline{M}\,\mu_L}\right)\frac{\varepsilon_{inter}\,\overline{d}_C^{\,2}\,P_v^C}{\ell_{ZA}} + \frac{\varepsilon_{inter}\,\overline{d}_C}{3\,\ell_{ZA}}\left[\sum_{I=1}^{N}\sqrt{\frac{8}{\pi M_i\,RT}}\left(P_{v,i}^C - P_{v,i}\right)\right]$$

(Eq. VI.71)

From Eqs. VI.70 and VI.71, the mean size and the intercrystalline porosity can be determined by Eqs. VI.72 and VI.73

$$\overline{d}_C = \frac{\lambda\left(\frac{32\,\overline{M}\,\mu_L}{\rho_L}\right)\left[\sum_{I=1}^{N}\sqrt{\frac{8}{\pi M_i\,RT}}\left(P_{v,i}^C - P_{v,i}\right)\right]}{3\left(\varphi - N^S + \lambda\,P_v^C\right)}\ [\text{nm}] \qquad \text{(Eq. VI.72)}$$

$$\varepsilon_{inter} = \frac{9\,\ell_{ZA}\left(\varphi - N^S + \lambda\,P_v^C\right)^2}{\lambda\left(\frac{32\,\overline{M}\,\mu_L}{\rho_L}\right)\left[\sum_{I=1}^{N}\sqrt{\frac{8}{\pi M_i\,RT}}\left(P_{v,i}^C - P_{v,i}\right)\right]^2}\ [-] \qquad \text{(Eq. VI.73)}$$

Finally, the likelihood that a defect is present in the layer can be calculated as the first moment of the PSD of the defects, $\langle d_C^1 \rangle$ [nm], according to Eq. VI.74

$$\langle d_C^1 \rangle = \varepsilon_{inter}\,\overline{d}_C = \frac{3\,\ell_{ZA}\left(\varphi - N^S + \lambda\,P_v^C\right)}{\left[\sum_{I=1}^{N}\sqrt{\frac{8}{\pi M_i\,RT}}\left(P_{v,i}^C - P_{v,i}\right)\right]}\ [\text{nm}] \qquad \text{(Eq. VI.74)}$$

VI.2.2. Characterization of intercrystalline porosity in zeolite NaA membranes by VPV

The general ideas pointed out in section VI.2.1 are used in this section for the characterization of intercrystalline porosity in for some inner-side tubular zeolite NaA membranes synthesized in this work (see chapter IV). The main characteristics of the membranes used in the present study are summarized in Table VI.4. Zeolite NaA membranes with different VPV performance towards the separation of ethanol/water mixtures were selected in order to assess differences in intercrystaline porosities in the zeolite NaA layers.

For each membrane, a set of steady-state VPV experiments for the separation of an ethanol/water liquid mixture (8.05-9.16 wt.% water) at 323 K were carried out for the liquid feed pressure range 1-8 bar. The evolution of the total flux, $\mathbf{N^T}$ [kg m^{-2} h^{-1}], and the water/ethanol selectivity [-] with the feed pressure for the membranes listed in Table VI.4 is plotted in Figures VI.11 and VI.12. As can be seen in Figure VI.11, the total flux obtained in the VPV experiments tends to increase linearly with the feed pressure for all the membranes tested except for the latter, ZA6, which showed no dependence on the feed

Table VI.4: Zeolite NaA membranes used in the present study. PV conditions: X_w= 8.05-9.16 wt.% (x_w = 0.18-0.20); T=323 K; P_o =1-3 bar (100-300 kPa); P_v =1-3 mbar (100-300 Pa)

Membrane	*Code (see Table IV.3)*	*Y_W (perm.) [-]*	*$\alpha_{W/E}$ [-]*	*N^T [kg m^{-2} h^{-1}]*
ZA1	**ZA-INN-02**	0.1360	2	2.44
ZA2	**ZA-INN-CF -09**	0.6642	20	0.51
ZA3	**ZA-INN-CF -05**	0.9421	185	0.58
ZA4	**ZA-INN-CF-03**	0.9811	294	0.36
ZA5	**ZA-INN-SC-18**	0.9900	1084	0.47
ZA6	**ZA-INN-C-05**	0.9984	8538	0.83

pressure. The reproducibility of the experiments was excellent, since standard deviations lower than 5% and 10%, respectively, were obtained for both the total flux and the water/ethanol selectivity. The linear trends observed for the total flux with the feed pressure for most of the membranes reported in Table VI.4 sustain the idea that Eq. VI.69 is suitable for the characterization of the intercrystalline porosity of the tested membranes. It should be highlighted that the contribution of the support to the overall mass transfer computed from the total fluxes was lower than 1% for all the membranes for the range of experimental conditions tested, which also sustains the application of the set of Eqs. VI.72 and VI.73 to determine intercrystalline data. Moreover, Figure VI.12 reflects a decrease in the water/ethanol selectivity with the feed pressure, which might involve a higher role of large defects compared to surface diffusion in zeolite pores that might partially compensate the ability of the latter to discriminate water from ethanol. The contribution of surface diffusion through zeolite pores to the overall mass transfer at each feed pressure can be determined by assuming that ethanol is not transferred through zeolite pores, that is, all the ethanol present at the permeate of the membrane in a VPV experiment is ascribed to mass transfer through large pores.

Moreover, mass transfer through large pores is assumed to be non-selective despite the slightly selective Knudsen diffusion contributions in zones II and III and vaporization at position C (see Figure VI.10). The surface diffusion flux, essentially related to water surface diffusion through zeolite pores, can be thus approached to Eq. VI.75

$$N_w^S = \text{total water transferred} - \text{water transferred through large pores} \approx$$

$$\approx Y_w N^T - Y_E N^T \frac{Y_w^C}{Y_E^C} = \left(Y_w - Y_E \frac{y_w^C}{y_E^C} \frac{M_w}{M_E} \right) N^T = \left(Y_w - Y_E \frac{a_w^C P_w^o}{a_E^C P_E^o} \frac{M_w}{M_E} \right) N^T =$$

$$= \left(Y_w - Y_E \frac{a_w P_w^o}{a_E P_E^o} \frac{M_w}{M_E} \right) N^T \approx Y_w N^T \quad [\text{kg m}^{-2} \text{h}^{-1}], \qquad \text{(Eq. VI.75)}$$

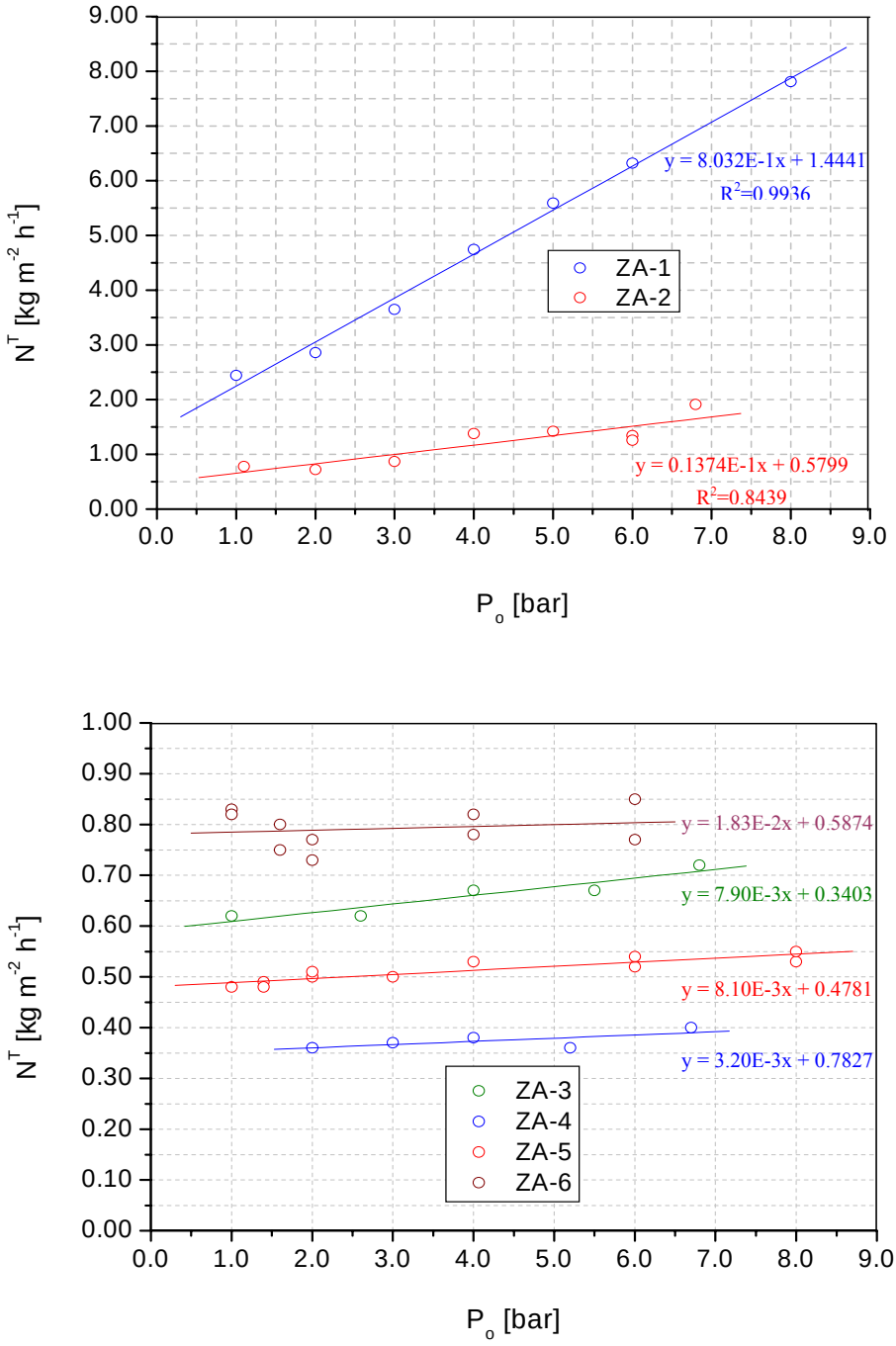

Figure VI.11: Total flux vs. feed pressure in the VPV of ethanol/water mixtures for the zeolite NaA membranes listed in Table VI.4.

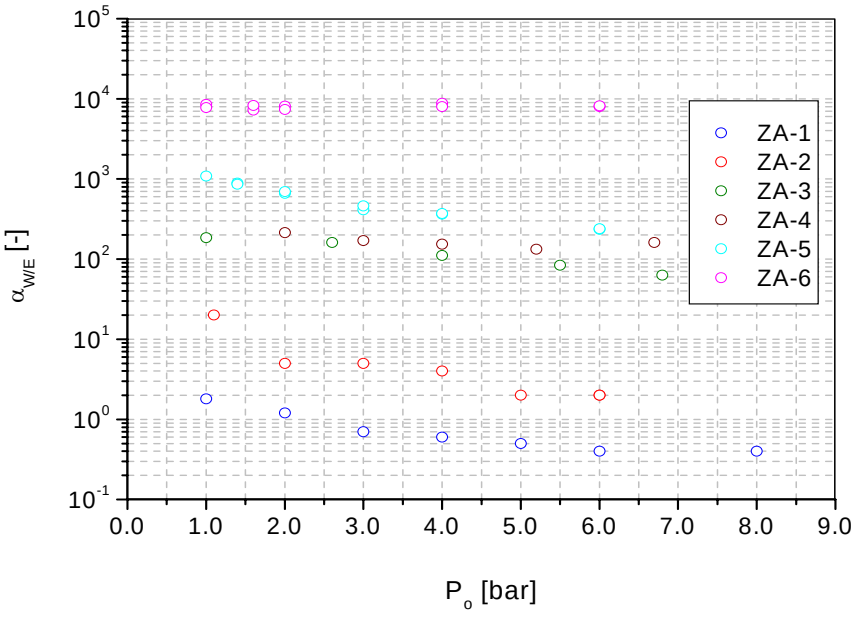

Figure VI.12: Water/ethanol selectivity vs. feed pressure in the VPV of ethanol/water mixtures for the zeolite NaA membranes listed in Table VI.4.

where $\mathbf{X_i}$ and $\mathbf{Y_i}$ are the weight fractions [-] of species **i** at the feed and permeate sides of the membrane, respectively, and y_i^C is the molar fraction of species **i** at position C (see Figure VI.10). Figure VI.13 shows the evolution of the surface diffusion flux determined by Eq. VI.75 with the feed pressure in the VPV experiments for the membranes listed in Table VI.4.

From the trends observed in Figures VI.12-VI.13, the mean pore size and intercrystalline porosity can be determined by using Eqs. VI.72 and VI.73. Tables VI.5-VI.7 summarize relevant physical data, and the data corresponding to intercrystalline porosity obtained from the present model. As can be seen in Table VI.7, the mean pore sizes computed for all the membranes are in the range 3.5-17.6 nm, which lie in the mesopore range (2-50 nm), while the intercrystalline porosity shows higher values for the membranes with lower water/ethanol selectivities. Figure VI.14 shows the evolution of the likelihood of defects with the water/ethanol selectivity in a double-log plot. As can be seen, the selectivity tends to be strongly reduced with the likelihood of defects. For practical purposes, the empirical equation VI.76 allows to estimate the likelihood of defects given the water/ethanol selectivity of an *as*-synthesized inner-side tubular zeolite NaA membranes with the experimental protocols described in chapter IV

$$\alpha_{w/E}\,[-] = \mathrm{Exp}\left[-0.94\,\mathrm{Ln}\left(\langle d_C^1\rangle\,[\mathrm{nm}]\right) - 0.076\right], \qquad \text{(Eq. VI.76)}$$

where $\alpha_{w/E}$ is the water/ethanol selectivity [-].

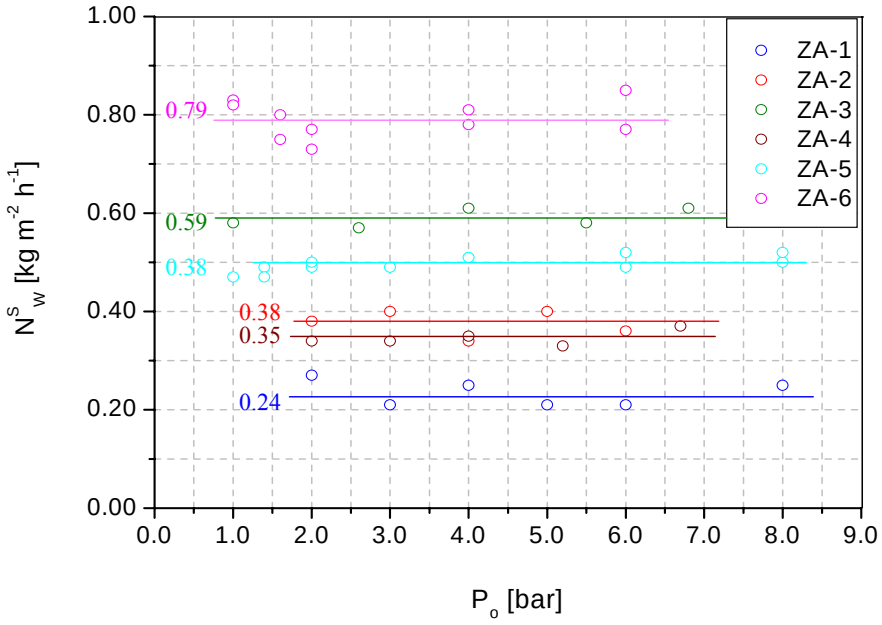

Figure VI.13: Evolution of the surface diffusion flux with the feed pressure in the VPV of ethanol/water mixtures for the zeolite NaA membranes listed in Table VI.2.

Table VI.5: Data used in the computations (X_w = 8.05-9.16 wt.%; T = 323 K)

Parameter *	***Range***
$\overline{M}$ x10^3 [kg mol^{-1}]	40.53 – 41.03
ρ_L [kg m^{-3}]	768.2 – 771.6
∇ x10^3 [mol m $^{-3}$]	1.85 – 1.90
μ_L x10^4 [kg m^{-1} s^{-1}]	7.04 – 7.11
P^o [kPa]	27.5

* Data for a water/ethanol mixture at 323 K (from *Weast, 1971*)

Table VI.6: Data used in the computations. VPV conditions as in Table VI.5

	ZA1	*ZA2*	*ZA3*	*ZA4*	*ZA5*	*ZA6*
λ (EXP) x10^3 [kg m^{-2} h^{-1} bar^{-1}] (1)	803.2 ± 28.7	13.7 ± 3.6	18.3 ± 1.0	7.9 ± 1.2	8.1 ± 3.0	3.22 ± 1.5
λ (EXP) x10^9 [mol m^{-2} s^{-1} Pa^{-1}]	53.8	11.6	1.22	0.522	0.345	0.0594
φ (EXP) x10^2 [kg m^{-2} h^{-1}] (1)	144.4 ± 13.5	58.0 ± 7.3	58.7 ± 0.9	34.0 ± 4.8	47.8 ± 1.4	78.3 ± 5.4
φ (EXP) x10^4 [mol m^{-2} s^{-1}]	81.1	6.51	1.06	79.5	0.439	0.0936
N^S [kg m^{-2} h^{-1}] (2)	0.24 ± 0.03	0.38 ± 0.02	0.59 ± 0.01	0.35 ± 0.02	0.49 ± 0.03	0.79 ± 0.04
ℓ_{ZA} [µm] (3)	50	30	35	30	35	7
D_L x10^{11} [m^{-2} s^{-1}]	723	932	9.85	4.26	2.78	0.479

[1] From Figure VI.6 (Confidence interval for probability level of 95%)
[2] From Figure VI.8
[3] From SEM analysis

Table VI.7: Results for the calculations with the proposed model for input data in Table VI.6

Variable	*ZA1*	*ZA2*	*ZA3*	*ZA4*	*ZA5*	*ZA6*
$\bar{d}_C$ [nm] [1]	9.7 ± 4.0	17.6 ± 13.9	15.1 ± 8.0	9.7 ± 3.0	15.9 ± 7.1	3.5 ± 1.6
ε_{inter} x10^4 [-] [1]	346 ± 73	9.8 ± 6.3	1.9 ± 0.8	2.0 ± 1.0	0.76 ± 0.2	0.14 ± 0.07
$<\bar{d}_C^1>$ x10^4 [nm]	3356 ± 71	188 ± 11	29.3 ± 1.3	19.7 ± 9.5	12.2 ± 2.7	0.49 ± 0.31
$D_{Kn,W}$ x10^{10} [m^2 s^{-1}]	687	41.4	6.03	4.04	2.28	0.478
$D_{Kn,E}$ x10^{10} [m^2 s^{-1}]	430	25.9	3.77	2.53	1.42	0.299
$P^C_{v,W}$ [kPa][2]	5.04	5.27	4.93	5.00	5.43	4.45
$P^C_{v,E}$ [kPa][2]	22.4	22.2	22.6	22.5	22.1	23.0
z_L [-][2]	0.29	0.47	0.39	0.29	0.32	0.29
N_I^V x10^4 [mol m^{-2} s^{-1}][2]	136	18.2	2.30	1.33	0.788	0.0154
N_{II}^{Kn} x10^4 [mol m^{-2} s^{-1}][2]	136	18.2	2.30	1.33	0.788	0.0154

[1] Confidence interval for probability level of 95%
[2] Computed at P_o=1.0 bar

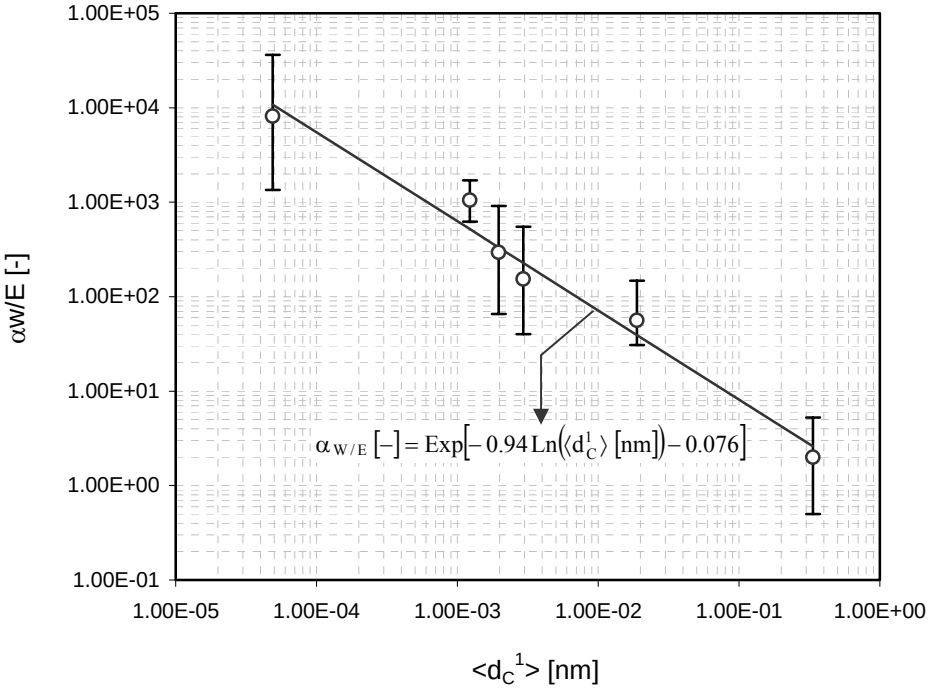

Figure VI.14: Evolution of the water ethanol selectivity with the likelihood of defects in the VPV of ethanol/water mixtures for the zeolite NaA membranes listed in Table VI.4.

VI.3. DISCUSSION AND FINAL REMARKS

In section VI.1, a mathematical model has been presented and experimentally validated to predict pore size distributions (PSDs) in meso- and macroporous asymmetric membranes for MF, UF and NF applications by using moment theory. The input data supplied to the model consist of three independent permeation experiments: (1) single gas diffusion permeance at low pressure, (2) pure liquid permeability, and (3) non-hindered diffusion of a species (e.g. an electrolyte). The latter experiment only provides data related to the support because of the higher contribution to the overall mass transfer for these experiments. Due to these strong limitations, for UF and NF membranes, only the mean diameter $\overline{d}_{M,2}$ and the porosity of the support, ε_S / τ_S, can be experimentally determined. The great advantage of the method relies on the possibility to characterize membranes in terms of their permeation behavior instead of the traditional characterization by molecular weight cutoff values (MWCO). Moreover, the method allows to overcome the shortcomings related to low sample representativity of microscopic techniques (e.g., SEM, TEM, FESEM and AFM) and also allows to distinguish between dead-end pores and active pores to permeation, which cannot be

usually distinguished by techniques such as permporometry and mercury porosimetry. On the other hand, compared to the latter two techniques, the method does not involve the use of the Kelvin equation, which shows a strong limitation for pores <5-10 nm. Therefore, pores in this range and even lower, in the nearby of the micropore range (2-10 nm) can be also in principle subjected to characterization by the present method.

The present method has been extended in section VI.2 to characterize large defects in zeolite NaA layers in the meso- and macroporous range from a collection of VPV experiments performed for the separation of ethanol/water mixtures at feed (retentate) pressures in the range 1-8 bar. Structural information concerning large pores in zeolite NaA layers can be obtained from the intercept and slope of the curve that describes the evolution of the total flux permeated through a zeolite NaA membrane with the liquid feed pressure. In light of the results presented in this section, the zeolite NaA membranes synthesized in our laboratory lose partially their separation ability to dehydrate ethanol/water liquid mixtures for intercrystalline porosities $>10^{-3}$ [-]. Moreover, although a zeolite membrane shows good PV performance towards the dehydration of organic mixtures, the presence of a small number of meso- and macroporous defects in the zeolite layer cannot be ruled out, which might cause a reduction of the selectivity of the membranes.